Constraints for the Martian Crustal Structure From Rayleigh Waves Ellipticity of Large Seismic Events

Jing Shi, Tao Wang, Han Chen, Minghan Yang, Ling Chen, Hejiu Hui, Zongbo Xu, Philippe Lognonné, Taichi Kawamura

JGR Planets

RESEARCH ARTICLE
10.1029/2022JE007676

Key Points:

- The stability of a *P*-wave receiver function degrades with increasing fractional velocity fluctuation of the shallow crust
- The fractional velocity fluctuation of the shallow crust is larger on the Moon than on Earth and Mars
- The water content of the crustal rocks is the main factor responsible for the different fractional velocity fluctuations

Supporting Information:

Supporting Information may be found in the online version of this article.

Correspondence to:

T. Wang,
twang0630@gmail.com

Citation:

Shi, J., Wang, T., Chen, H., Yang, M., Chen, L., Hui, H., et al. (2023). Differences in scattering properties of the shallow crusts of Earth, Mars, and the Moon revealed by *P*-wave receiver functions. *Journal of Geophysical Research: Planets*, *128*, e2022JE007676. https://doi.org/10.1029/2022JE007676

Received 13 NOV 2022
Accepted 13 JUL 2023

Author Contributions:

Conceptualization: Tao Wang
Formal analysis: Jing Shi, Tao Wang, Han Chen, Minghan Yang, Ling Chen
Methodology: Jing Shi
Supervision: Tao Wang
Validation: Jing Shi
Writing – original draft: Jing Shi
Writing – review & editing: Jing Shi, Tao Wang, Han Chen, Minghan Yang, Ling Chen, Hejiu Hui, Zongbo Xu, Philippe Lognonné, Taichi Kawamura

Differences in Scattering Properties of the Shallow Crusts of Earth, Mars, and the Moon Revealed by *P*-Wave Receiver Functions

Jing Shi[1,2], Tao Wang[1], Han Chen[1], Minghan Yang[1], Ling Chen[3,4], Hejiu Hui[1,5], Zongbo Xu[2], Philippe Lognonné[2], and Taichi Kawamura[2]

[1]Frontiers Science Center for Critical Earth Material Cycling, School of Earth Sciences and Engineering, Nanjing University, Nanjing, China, [2]Institut de physique du globe de Paris, Université Paris Cité, CNRS, Paris, France, [3]State Key Laboratory of Lithospheric Evolution, Institute of Geology and Geophysics, Chinese Academy of Sciences, Beijing, China, [4]College of Earth and Planetary Sciences, University of Chinese Academy of Sciences, Beijing, China, [5]Center for Excellence in Comparative Planetology, Chinese Academy of Sciences, Hefei, China

Abstract The scattering properties of terrestrial planetary bodies can provide valuable insights into their shallow seismic structure, meteoritic impact history, and geological activity. Scattering properties of the shallow crusts of Earth, Mars, and the Moon are investigated by constructing *P*-wave receiver functions (PRFs) from teleseismic waveforms with high signal-to-noise ratios. The authors' analysis reveals that strong coda waves lead to significant variations in the PRF waveforms calculated using different time windows, and the stability of the PRF is primarily influenced by the fractional velocity fluctuation. Synthetic PRFs for various scattering media confirm these observations. Comparing the observed and synthetic PRFs, it is found that the fractional velocity fluctuation in the shallow crust is greater than ~0.2 for the Moon but less than ~0.2 for Earth and Mars. The authors further discuss possible mechanisms that could have affected the fractional velocity fluctuation and suggest that the distinct fractional velocity fluctuation between the Moon and Earth/Mars is mainly due to differences in the water content of the crustal rocks of the three planetary bodies.

Plain Language Summary Coda waves follow direct *P* or *S* waves and comprise scattered waves generated when seismic waves travel through a heterogeneous medium. These incoherent coda waves may interfere with seismic waves from coherent structures and complicate the interpretation of seismic structures. The authors compute *P*-wave receiver functions (PRFs) of Earth, Mars, and the Moon using teleseismic waveforms with high signal-to-noise ratios. It is found that the PRFs of Earth and Mars are reliable and that the crustal converted waves can be effectively recovered. However, the PRF of the Moon calculated using different time windows is unstable even for direct *P* waves. The authors demonstrate that the stability of the PRF can be used to characterize the strength of the seismic scattering. Increased scattering by the medium leads to the degradation of the PRF stability. The PRF stability is mainly affected by the fractional velocity fluctuation of the shallow crust, which is larger on the Moon than on Earth and Mars. The fractional velocity fluctuation of the shallow crust is smaller on Earth and Mars because their shallow crusts are hydrous, whereas the shallow crust of the Moon is anhydrous.

1. Introduction

Seismic scattering refers to the redirection and deflection of seismic waves caused by heterogeneities or irregularities inside a planetary body. When seismic waves encounter changes in the properties of rocks, such as density, porosity, and elasticity, they can be scattered in different directions (Margerin, 2011). Characterizing and investigating seismic scattering in the shallow crust is crucial for understanding the evolutionary history of terrestrial planetary bodies as it reveals subsurface structural heterogeneity, primarily determined by meteoritic impacts or geological activity (Latham et al., 1970; Sato et al., 2012). Meteoritic impacts can crush the shallow crust, increase porosity, and enhance seismic scattering. Additionally, seismic scattering is also influenced by geological activity; for example, many pyroclastic rocks are accumulated in the volcanic area by the volcanism and act as scatterers, resulting in seismic scattering (Kumagai et al., 2018).

One of the effects of seismic scattering is the formation of coda waves, which are wave trains that follow direct *P* or *S* waves and are generated in a heterogeneous medium (Aki & Chouet, 1975; Sato et al., 2012). Coda waves

in seismograms of Earth and Mars typically last a few to dozens of minutes (Lognonné et al., 2020), while those of the Moon can last 1–2 hr, indicating more intense seismic scattering (Garcia et al., 2019). Scattered waves can interfere with seismic signals related to interior interfaces, causing phase distortion. However, measuring whether the seismic phase is true in such a highly scattering medium remains unclear.

The seismic scattering is mainly controlled by the correlation length of the scatterer (a) and the fractional velocity fluctuation (ε) of a scattering medium (Sato et al., 2012). The medium is considered to be approximately homogeneous when a is much smaller than the wavelength, whereas the scattering of the medium is strong when a is comparable to the wavelength. Meanwhile, the ε is a measure of the heterogeneity of the medium, and the larger the ε, the stronger the seismic scattering (Sato et al., 2012). Sato (2019) compiles results from various studies and shows that the Earth's crust has ε values of ~0.01–0.2 (Flatté & Wu, 1988; Fukushima, 2003; Nakata & Beroza, 2015; Wu et al., 1994). However, there have been no reports on ε values for the Martian crust. For the Moon, Weber et al. (2015) generated seismograms similar to real moonquake records by setting the velocity fluctuation of the megaregolith to a value of 0.25. Onodera et al. (2021) constrain the scattering megaregolith thickness to 10–20 km beneath the Apollo 12 station by setting the velocity fluctuation of the regolith (0.28) and the megaregolith (0.14), and by fitting the rise-coda of two artificial impacts. However, Onodera et al. (2021) do not discuss other Apollo stations, and the estimation of the megaregolith thickness may have a trade-off with the velocity fluctuation, which remains controversial (Blanchette-Guertin et al., 2015; Zhang et al., 2022). Last but not least, no study has yet compared the ε values of Earth, Mars, and the Moon in the same methodological framework.

In this study, we use the *P*-wave receiver function (PRF) (Langston, 1979; Ligorria & Ammon, 1999) to constrain the scattering properties of the shallow crusts of Earth, Mars, and the Moon. We choose the PRF method for the following four reasons. (a) The PRF is a common method to study the seismic structures of a planetary body (e.g., Durán et al., 2022; Knapmeyer-Endrun et al., 2021; Lognonné et al., 2020; Vinnik et al., 2001; Zhu & Kanamori, 2000), but whether the PRF is affected by the a and the ε of a scattering medium, which may reflect the mechanism and evolution process, is unknown. (b) The scattered waves in the scattering medium vary in different time windows, but it is unclear whether the PRFs are stable when calculated using different time windows. (c) The PRF method is widely used to study seismic structures of various scales on Earth (e.g., Victor et al., 2020; Xu et al., 2018; Zhu & Kanamori, 2000) and has also been successfully applied to Mars (Durán et al., 2022; Knapmeyer-Endrun et al., 2021; Lognonné et al., 2020; Shi et al., 2023a). However, for the Moon, only *S-wave receiver functions* beneath Apollo 12 (Lognonné et al., 2003; Vinnik et al., 2001) and no other RFs have been retrieved. This knowledge gap is worth investigating to determine whether it is due to the strong seismic scattering of the Moon. (d) The PRF is mainly sensitive to the structure in the vicinity of the station. The PRF calculation does not require prior information, such as the source time function, the exact source location, or the velocity model.

The rest of this paper is organized as follows. Section 2 describes the data and preprocessing. Then, in Section 3, we investigate the effects of different computational time windows on the PRF retrieval, stack PRFs calculated from multiple time windows, and compute synthetic PRFs with varying scattering media to assess the scattering properties of the shallow crusts of Earth, Mars, and the Moon. Lastly, in Section 4, we discuss potential factors that could affect the results and analyze the mechanisms for the differences in the scattering properties of the three planetary bodies.

2. Data and Preprocessing

To investigate analogous terrestrial environments to those of Mars and the Moon, we collect broadband seismic stations from seven sites (Figure 1a), which have been identified as the best planetary field analogs based on the evaluation conducted by the Europlanet society (Thompson & Cane, 2022). (a) The Andes Mountains in the Puna region of Argentina (Argentinian Andes (AA) in Figure 1a) are characterized by high UV influx, an arid climate with little water, extreme diurnal temperature fluctuations (>40°C), strong winds (up to 400 km/hr), and a geological environment dominated by volcanoes. All these features make this region an ideal planetary analog for the environments of Mars and other icy planets/moons. (b) The AU Kangerlussuaq Field Site (AK in Figure 1a) is at the west of Greenland, one of the few truly extremely cold environments on Earth. (c) The Iceland Field Sites-Matis (IM in Figure 1a) has a variety of environments, including lava fields of various ages, volcanic areas, active hydrothermal systems, and glacial and subglacial environments. (d) The Rio Tinto (RT)'s hydrated mineral

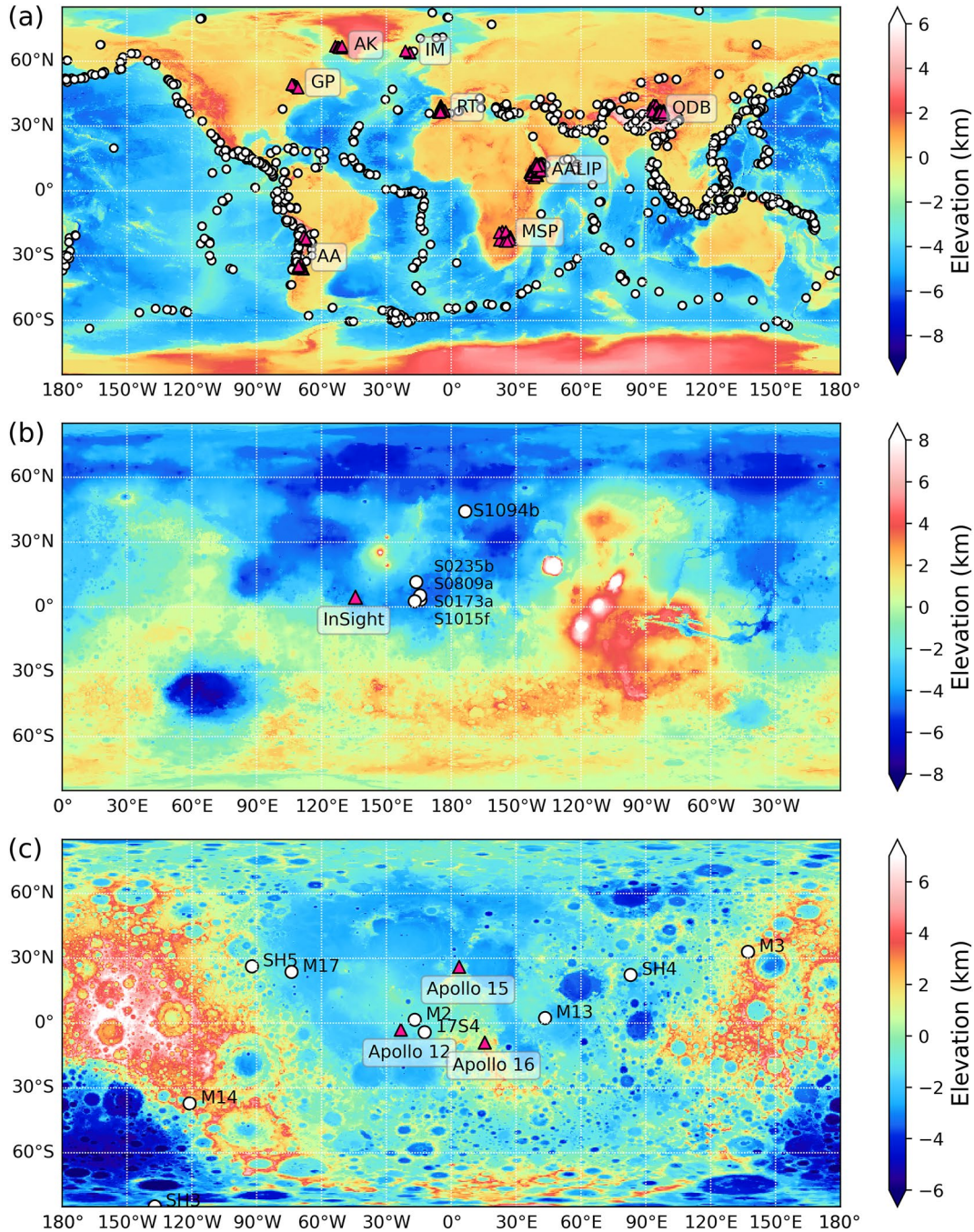

Figure 1. Distribution of used seismic events and stations. The white circles represent the selected events, while the red triangles represent the seismic stations. Maps of Earth (a) (National Geophysical Data Center, 1993), Mars (b) (Smith et al., 2001), and the Moon (c) (Smith et al., 1997) depict the projected locations of these seismic events and stations. On the Earth map, we mark the locations of the eight planetary field analogs, namely the Grenville Province, the Argentinian Andes, the AU Kangerlussuaq Field Site (AK), the Iceland Field Sites-Matis (IM), the Rio Tinto, the Makgadikgadi Salt Pans, the Afro-Arabian Large Igneous Province, and the Qaidam Basin (QDB). We also mark the name of each seismic event on the maps of Mars and the Moon. For moonquakes, M and SH represent the meteoritic impact and the shallow moonquake, respectively, and the 17S4 is an artificial impact event.

deposits (RT in Figure 1a) are dominated by jarosite and goethite, similar to those on Mars. (e) The Makgadikgadi (Makgadikgadi Salt Pans (MSP) in Figure 1a) has layered morphologies and evaporite deposits formed by water activity that can be compared to regions near the Martian equator. (f) The Afro-Arabian Large Igneous Province

(AALIP in Figure 1a) is characterized by extensive basaltic lava flows, as is the mare region of the Moon. (g) The Qaidam Basin (QDB in Figure 1a) is a high-altitude sedimentary basin with an ultra-arid climate, low annual average temperature (as low as 1.9°C), and large diurnal temperature fluctuations (up to 64°C). With many sedimentary deposits, ancient lakes, and rich landscape features, the Qaidam Basin provides an excellent analogy to the Martian environment. In addition, we include seismic stations from one additional site (Grenville Province, GP in Figure 1a) in eastern Canada with anorthosite massifs (Petrescu et al., 2016) to provide an analogy to the highlands of the Moon, which are mainly composed of anorthosite (Wieczorek et al., 2006).

On Mars (Figure 1b), we use the seismometer from the SEIS (Seismic Experiment for Interior Structure) of the InSight (the Interior Exploration using Seismic Investigations, Geodesy, and Heat Transport) mission (Banerdt et al., 2020). The InSight lander is located in the Elysium Planitia, the youngest volcanic area on Mars (Pan et al., 2020). This region is characterized by a large shield volcano (the Elysium Mons) and several smaller volcanic features, such as volcanic cones, fissure vents, and lava flows (Golombek et al., 2018). We can use the seismic scattering property at InSight's landing site to represent that of the northern lowlands of Mars, whereas there are no seismic data from the southern highlands, so we cannot constrain the seismic scattering property there.

On the Moon (Figure 1c), we selected seismometers from Apollo stations 12, 15, and 16 (Nunn et al., 2020). Apollo 12 and 15 are located in mare regions whose surface is covered by extensive basaltic rocks. It is believed that there was once a large number of volcanic activities in the mare regions (Jolliff et al., 2006). Apollo 16 is in the highlands, mainly composed of anorthosite formed during the cooling of the early lunar magma ocean. Volcanic activity in the highlands is generally less than in the mare regions (Jolliff et al., 2006). In addition, we do not use seismic data from Apollo stations 11 and 14 due to the short duration of operation for Apollo 11 and abnormal data for the vertical component of Apollo 14 (Nunn et al., 2020).

To appropriately calculate the PRF, the epicentral distance used in the calculation must meet specific criteria. To ensure a near-vertical incidence of the direct *P* wave (Langston, 1979; Ligorria & Ammon, 1999), the lower limit of the epicentral distance needs to be large enough. Moreover, the upper limit of the epicentral distance is usually determined to avoid the influence of the seismic phase from the core–mantle boundary, such as core-diffracted *P* waves (*Pdiff*). On Earth, the epicentral distance of the teleseismic event used to calculate the PRF is typically between 30 and 90°. However, for Mars and the Moon, we use different ranges based on their respective velocity models: 25°–90° for Mars (InSight_KKS21GP) (Khan et al., 2021; Knapmeyer-Endrun et al., 2021; Stähler et al., 2021), and 25°–140° for the Moon (VPRM: the very preliminary reference Moon model) (Garcia et al., 2011). These ranges ensure the near-vertical incidence of the direct *P* wave and a non-zero transmission coefficient of the converted *S* wave at the crust-mantle boundary (Figure S1 in Supporting Information S1).

For Earth, we collect seismic stations with seismic records over half a year from each planetary field analog and select teleseismic earthquakes with $Mw > 5.5$. For Mars, we collect marsquakes with location quality marked as A (i.e., epicentral distance and back azimuth are confidently estimated), according to the InSight Marsquake Service (2022). For the Moon, we collect two types of moonquakes—shallow moonquakes and impact events—whose locations are given by Garcia et al. (2011). We do not use deep moonquakes for two reasons. Firstly, the *P*-wave ground motion of a deep moonquake is usually weak compared with shallow moonquakes and impact events, which makes it challenging to identify the direct *P* wave of a deep moonquake (Nakamura, 2005) and results in a very weak *P*-to-*S* wave. Secondly, the waveform quality of *P* waves from deep moonquakes is usually poor and cannot be dramatically improved even by stacking deep moonquakes from the same cluster (i.e., the same source region). This is because few coherent *P* waves exist between different moonquakes from the same cluster. For example, deep moonquakes, which are from cluster A9 and are recorded in Apollo 12, exhibit a very low average correlation coefficient (<0.05) for *P* waves (the 100-s window before the direct *S* wave) between different events (Figure S2 in Supporting Information S1).

A PRF is generally obtained by deconvolving the vertical component from the radial component (Langston, 1979; Ligorria & Ammon, 1999). Thus, the three components of motion need to be rotated to the vertical–radial–transverse (ZRT) system. On Earth, the seismic stations are generally deployed as the vertical–north–east (ZNE) system. In the case of InSight's SEIS data, we correct the instrumental response because it slightly differs when using the UVW (the three seismic components of InSight's SEIS: BHU, BHV, and BHW) system (Lognonné et al., 2019). We then rotate the UVW system to the ZNE system according to the dip and azimuth of InSight's SEIS seismic sensors. In the case of moonquake data, we interpolate the original irregularly sampled records to a

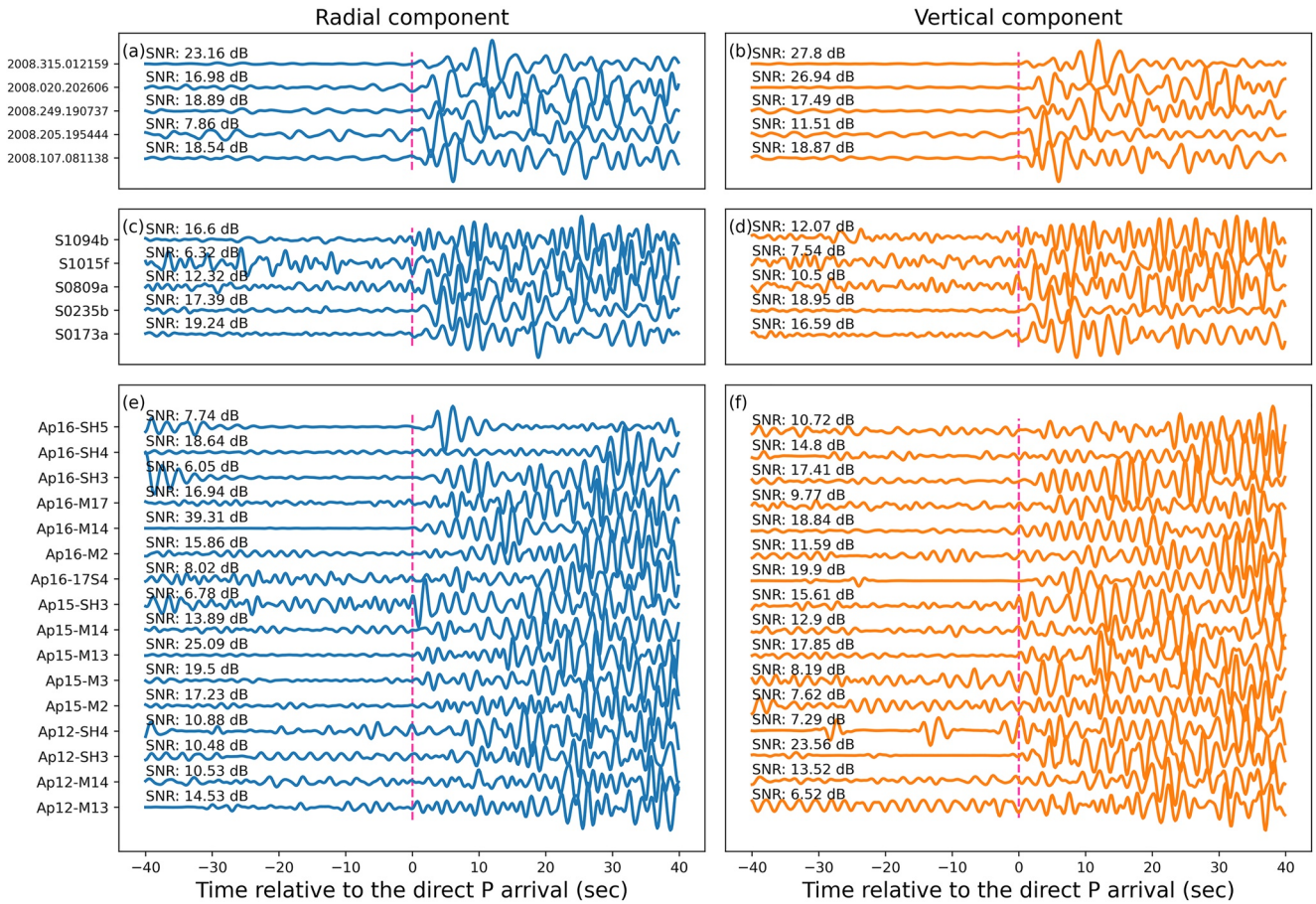

Figure 2. Radial (left column) and vertical (right column) seismic waveforms of selected events. (a) and (b) show examples of earthquake waveforms recorded by station BTIE in the Afro-Arabian Large Igneous Province, with corresponding *Y*-axis labels indicating the occurrence times of the seismic events. (c) and (d) are marsquake waveforms, with the *Y*-axis labeling the names of the seismic events. (e) and (f) present moonquake waveforms, with the *Y*-axis denoting the station and event pairs for each waveform. The *X*-axis is the arrival time relative to the direct *P* wave of each event (pink dotted line), and the left side of each waveform indicates the corresponding signal-to-noise ratio of the direct *P* wave.

consistent time interval of 0.151 s using cubic spline interpolation. We also correct the misaligned directions of Apollo 12 and 16 (Jarosch, 1977) to the ZNE system. We remove the linear trends and mean from all event waveforms and filter the waveforms with a 0.2–0.8 Hz Butterworth bandpass filter. Finally, we rotate the seismograms from the ZNE system to the ZRT system based on the back azimuth of each event and compute the radial PRF using the time-domain iterative deconvolution method (Ligorria & Ammon, 1999).

The quality of the *P*-wave waveform can significantly affect the recovery of converted waves. Thus, we only use events with high signal-to-noise ratio (SNR). We calculate the SNR of the direct *P* wave in the vertical and radial components for each event:

$$\mathrm{SNR} = 10 \cdot \log_{10}\left(\frac{A_S}{A_N}\right)^2, \tag{1}$$

where A_N and A_S are the root mean squares of the noise and signal waveforms (in 40-s windows before and after the direct *P* wave), respectively. Theoretical arrival times of direct *P* waves are determined using the IASP91 model (Kennett, 1991) for earthquakes and are provided by the InSight Marsquake Service. (2022) for marsquakes. For moonquakes, we calculate the theoretical arrival times of direct *P* waves using the catalog and the VPRM of Garcia et al. (2011). We select events only when the SNR of the direct *P* wave is larger than 6.0 dB for both the radial and vertical components to ensure the high waveform quality (Figure 2). In this paper, we select seismic events based on the SNR of the direct *P* wave instead of the magnitude, as the PRF is the response of the crustal structure near the station and is theoretically not affected by the energy of the seismic source. Table 1

Table 1
Detailed Information for All the Eight Planetary Field Analogs Used in This Study

Site No.	Lat (°)	Lon (°)	Rad (deg)	Network code:: Network name (time span used)	Ns	Ne	$\overline{MR}$
Region 1: Grenville Province, Canada							
1	48.5	−72.0	1.5	X8:: Deep structure of three continental sutures in Eastern North America (Quebec-Maine Array) (2014–2015)	8	254	$0.1^{\pm 0.03}$
Region 2: Argentinian Andes, Argentina*							
2	−36.0	−70.0	2.5	6A:: Teno Valley seismic network (TENO) (2017–2018)	18	611	$0.19^{\pm 0.06}$
				YC:: Slab geometry in the Southern Andes (Southern Andes) (2000–2002)			
3	−22.0	−67.0	2.5	YS:: The life cycle of Andean volcanoes: Combining space-based and field studies (ANDIVOLC) (2010–2012)	8	111	$0.24^{\pm 0.08}$
Region 3: AU Kangerlussuaq Field Site, Greenland							
4	67.0	−52.0	2.0	XK:: Seismic Arrays for African Rift Initiation (SAFARI) (2012–2015)	6	125	$0.18^{\pm 0.05}$
				NR:: The Network of Autonomously Recording Seismographs (NARS) (2014–2015)			
Region 4: Iceland Field Sites, Matis, Iceland*							
5	64.0	−21.0	1.5	XE:: Torfajokull 2002 (Torf2002) (2002–2002)	5	34	$0.18^{\pm 0.09}$
Region 5: Rio Tinto, CAB-CICS, Spain							
6	38.0	−5.0	1.5	XB:: Program to Investigate Convective Alboran Sea System Overturn (PICASSO) (2010–2012)	46	1,790	$0.19^{\pm 0.1}$
Region 6: Makgadikgadi Salt Pans, BIUST, Botswana							
7	−20.5	25.5	2.5	XK:: Seismic Arrays for African Rift Initiation (SAFARI) (2012–2015)	18	777	$0.12^{\pm 0.04}$
				NR:: The Network of Autonomously Recording Seismographs (NARS) (2014–2015)			
Region 7: Afro-Arabian Large Igneous Province, Ethiopia*							
8	11.5	42.0	4.0	ZF:: Afar Consortium Network (AFAR) (2008–2009)	45	3,477	$0.16^{\pm 0.07}$
				XI:: Seismic investigation of deep structure beneath the Ethiopian Plateau and afar depression (Ethiopia) (2001–2002)			
Region 8: Qaidam Basin, China							
9	38.0	92.0	3.0	X4:: Deep structure of the Northeastern Tibet collision zone: INDEPTH IV (ASCENT) (2008–2010)	27	3,393	$0.15^{\pm 0.1}$

Note. The table lists the central position (latitude: Lat, longitude: Lon) and the radius (Rad) of each site. The sites are listed in the order of longitude. Ns and Ne represent the number of seismic stations and events used at each site. $\overline{MR}$ denotes the average misfit reduction for the *P*-wave receiver function calculation in the corresponding planetary field analog, and the superscript is the 2σ uncertainty. Sites located in volcanic areas are marked with asterisks.

lists the number of selected earthquake events and seismic stations in each planetary field analog on Earth, and Figures 1a–1c show the retained earthquake, marsquake, and moonquake events.

3. Observations and Modeling

In this section, we analyze the effects of coda waves on the PRFs calculated using different time windows because of the distinct characteristics of the seismic coda waves on the three planetary bodies. We then evaluate the scattering properties of the shallow crusts of Earth, Mars, and the Moon based on the stability of the PRFs.

3.1. Effect of the Computational Time Window on the Retrieval of Stable PRFs

On Earth, the PRFs computed from different time windows are usually stable due to the rapid decay of coda wave amplitudes, so that the contribution of later coda waves is typically insignificant. The time window used

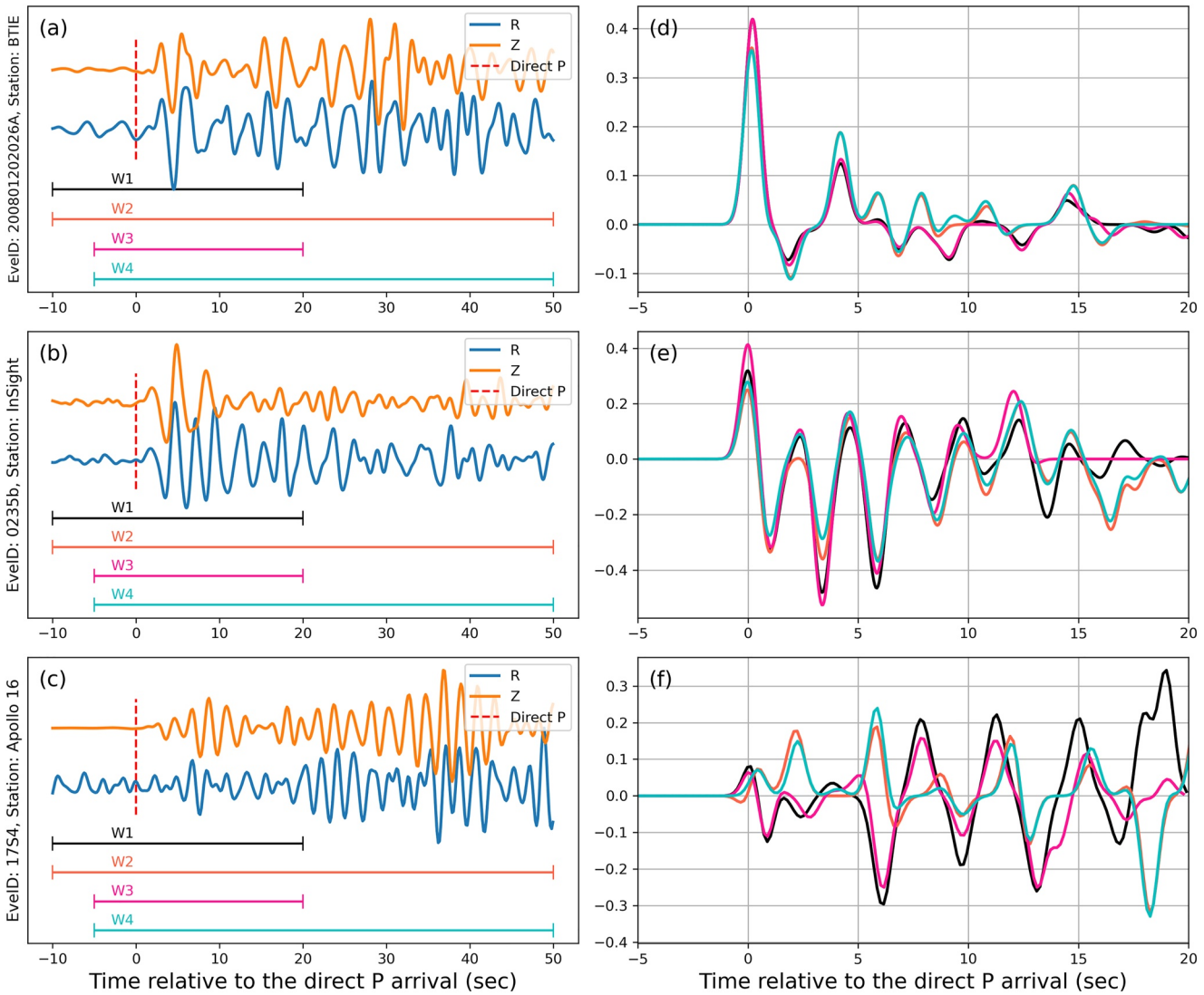

Figure 3. Examples of *P*-wave receiver functions (PRFs) of Earth, Mars, and the Moon are calculated using different time windows. The left column shows waveforms of the vertical (*Z*) and radial (*R*) components of a selected earthquake (a), marsquake (b), and moonquake (c). The waveforms are filtered at 0.2–0.8 Hz to eliminate low- and high-frequency noise. The dashed red line indicates the arrival time of the direct *P* wave, and the four different time windows used to compute the PRFs in (d)–(f) are marked by horizontal solid lines. The *Y*-axis labels the corresponding event and station. In the right column (d)–(f), the PRFs computed with the corresponding time window are displayed in the same colors as those used in (a)–(c). The *X*-axis shows the time relative to the arrival of the direct *P* wave.

to compute the PRF of Earth can be more than 100 s after a direct *P* wave to extract converted phases from deep interfaces, such as the 410- and 660-km discontinuities (e.g., Xu et al., 2018). For the Moon, however, it is uncertain whether the computational time window significantly affects the PRFs due to strong coda waves.

To investigate the effect of coda waves, we choose three seismic events (an earthquake, a marsquake, and a moonquake) as examples. The waveforms of the three events exhibit high SNRs (>8.0 dB) and are free of glitches, with clear identification of direct *P* waves (as shown in Figures 3a–3c). Then, we compute the PRFs using four different time windows for which the zero time corresponds to the arrival of the direct *P* wave: w1 (−10–20 s), w2 (−10–50 s), w3 (−5–20 s), and w4 (−5–50 s). Figure 3d shows that Earth's PRFs computed with different time windows are stable and have almost identical direct *P* waves and converted *S* waves (at ∼4 s) from the Moho (crust-mantle boundary). Figure 3e shows a slight variation for Mars' PRFs with various time windows. However, the Moon's PRFs vary depending on the time window (Figure 3f). Because there are few signals before the direct *P* wave, the start time has little effect on the Moon's PRFs, but the differences in PRFs computed with different end times are substantial. Therefore, it is reasonable to hypothesize that the instability of the Moon's PRFs is due to more scattering waves being involved as the length of the time window increases.

We compute synthetic PRFs of the Moon with different scattering media to test this hypothesis. We set up a two-layer crustal model where the first layer is heterogeneous and the second layer is homogeneous. The simulation includes a 10-km thick scattering layer with the crust-mantle boundary at a depth of 28 km, based on the VPRM of the Moon (Garcia et al., 2011) (see Table S1 in Supporting Information S1). We omit the first 1-km low-velocity layer from the VPRM because detection of the 1-km layer is beyond the resolution of our PRF and the thickness of the low-velocity layer is controversial (from zero to several kilometers) (Garcia et al., 2011, 2019; Onodera et al., 2021). We set a maximum frequency of 0.8 Hz to ensure the same as the real filtered data and then computed the 2D wavefield in the P-SV system using the procedure OpenSWPC (Maeda et al., 2017). To save computational cost, we place an explosion source (a Küpper wavelet) at a depth of 100 km below the receivers to generate a *P* wave that approximates the plane wave from teleseismic events. The grid width is 250 m and the time step width is 0.02 s. Meanwhile, the source duration time was 1.25 s. Our benchmark of PRFs for the layered homogeneous medium (Figure S3 in Supporting Information S1) shows that converted *P*-to-*S* waves of the two crustal discontinuities are recovered. The arrival times of converted and multiple waves are in good agreement with theoretical calculations, justifying the source setup and the correctness of the computed seismograms.

Subsequently, we set the random heterogeneity in the first layer and use the autocorrelation function (ACF) to describe the scattering medium. There are three common types of ACFs: Gaussian, exponential, and von Kármán, each with its mathematical expression (see Sato et al., 2012 for a review). In this study, we adopt the exponential ACF, which has been widely used in previous studies (Onodera et al., 2021; Sivaji et al., 2002) because it provides a simplified version of the von Kármán ACF and is more suitable for modeling short-wavelength random media compared to the Gaussian ACF (Sato et al., 2012). The exponential ACF is expressed as follows:

$$\langle \xi(x)\xi(x+r)\rangle = \varepsilon^2 \cdot e^{-r/a}, \tag{2}$$

where r represents the lag distance, and the angle brackets denote the integration over x (Sato et al., 2012). Since the wavelength is 3,600 m, we set two values for the correlation length of the scatterer (a): 1,000 m when it is less than half a wavelength and 4,000 m when it is comparable with a wavelength. And we test the combination of a with the fractional velocity fluctuation (ε) of 0.1 and 0.2. Finally, we compute seismograms for a ground receiver with a ray parameter of ∼0.08 s/km, which corresponds to the average ray parameter of the selected moonquakes and calculate the PRFs by deconvolving the vertical trace (*P*) from the radial trace (SV) (Ligorria & Ammon, 1999).

Figure 4 shows the seismograms and corresponding PRFs of four distinct scattering media. These results reveal how heterogeneity can introduce scattered waves into coda waves, leading to unstable PRFs when calculated with different time windows. For weak scattering ($\varepsilon = 0.1$), the PRF calculated with different time windows is relatively stable. However, for strong scattering ($\varepsilon = 0.2$), the stability of the PRF deteriorates. Furthermore, the PRF may have spurious signals, and the direct *P* wave may have a negative polarity. The instability of the PRF in the presence of strong scattering can be attributed to two reasons. Firstly, the amplitude of the later scattered waves is substantial, and the scattering effect for a long time window cannot be ignored. Secondly, an essential assumption for the PRF calculation is that the structural Green's function of the vertical component near the station can be approximated as a Dirac delta function (Langston, 1979). However, this assumption does not hold when the scattering is strong, as the *P* wave is contaminated by scattered waves.

3.2. Stacked PRFs on Earth, Mars, and the Moon

Given that in the case of intense seismic scattering, the calculated PRF may vary significantly depending on the time windows used, as shown above. Thus, to obtain a reliable PRF for each event, we compute 85 PRFs using 85 different time windows ranging from 10 s before to 15–100 s after the direct *P*-wave arrival, with a 1-s interval. We then average all 85 PRFs to obtain the stacked PRF waveforms of each event (Figure 5). In addition, to quantitatively evaluate the reliability of the PRF and how well the real radial component has been recovered, we calculate the misfit between the predicted (convolving of the real vertical component with the PRF) and real radial components (Ligorria & Ammon, 1999). We define the misfit reduction (MR) for the last iteration of the PRF calculation as follows:

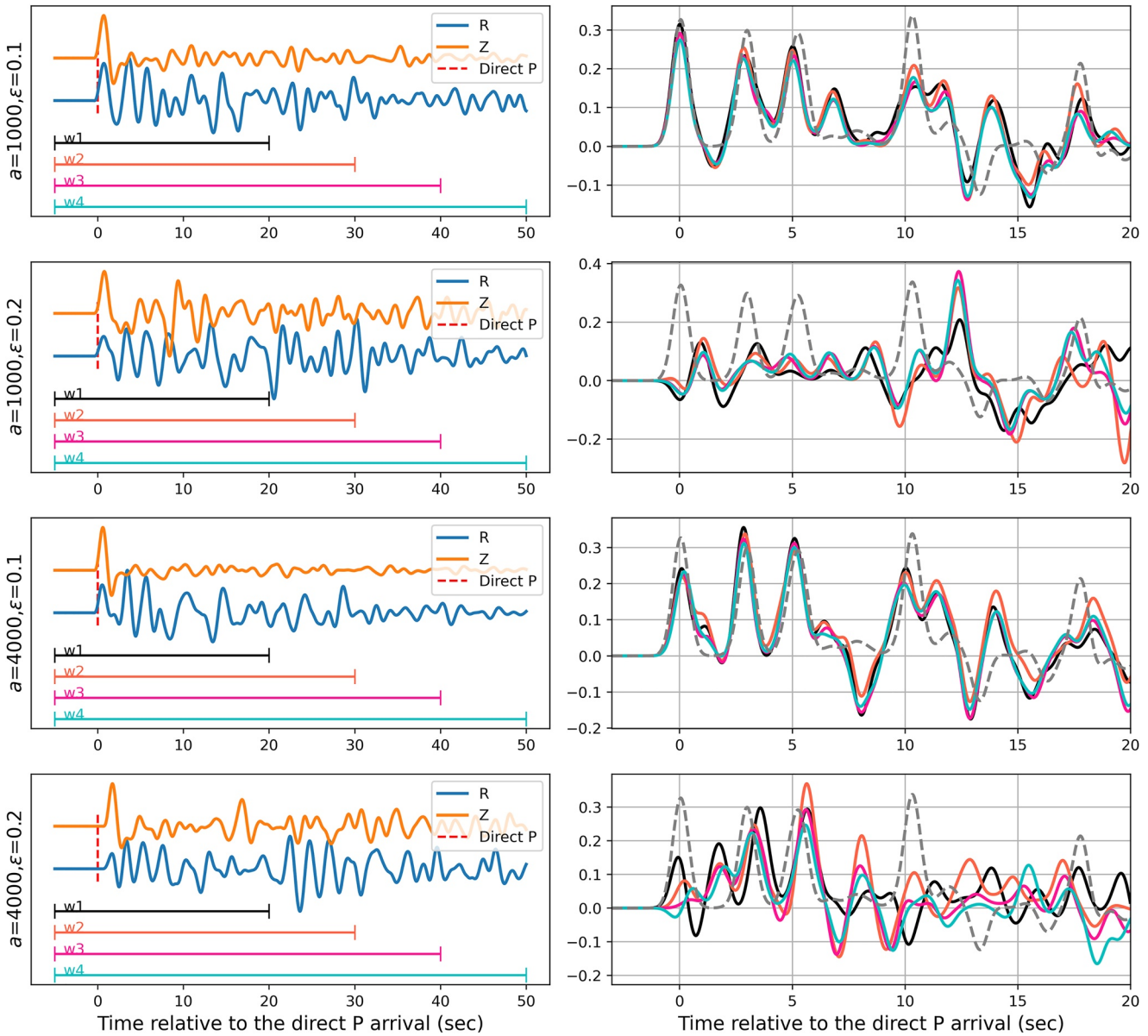

Figure 4. The left column displays radial (R) and vertical (Z) synthetic seismograms for different scattering media (a: correlation length and ε: fractional velocity fluctuation), with the theoretical arrival time of the direct P wave marked by the dashed red line. The right column shows synthetic P-wave receiver functions (PRFs) computed using time windows of different lengths. We use four different time windows (w1: −5–20 s, w2: −5–30 s, w3: −5–40 s, and w4: −5–50 s). The PRFs in the right column are displayed in the same color as the corresponding time windows in the left column. The dashed gray line in the right column represents the synthetic PRF without the influence of scattering, serving as a reference for comparison.

$$\begin{cases} \mathrm{MR} = \dfrac{\sum_{i}^{n} \left(R_i^p - R_i^o\right)^2}{\sum_{i}^{n} \left(R_i^o\right)^2}, \\ R^p = \mathrm{PRF} * Z \end{cases} \tag{3}$$

where Z is the real vertical component, and R_i^p and R_i^o are the predicted and real radial components. i and n denote the ith sampling point and sampling number. The larger the MR, the less convergence of the predicted radial component and the less reliable the PRF is.

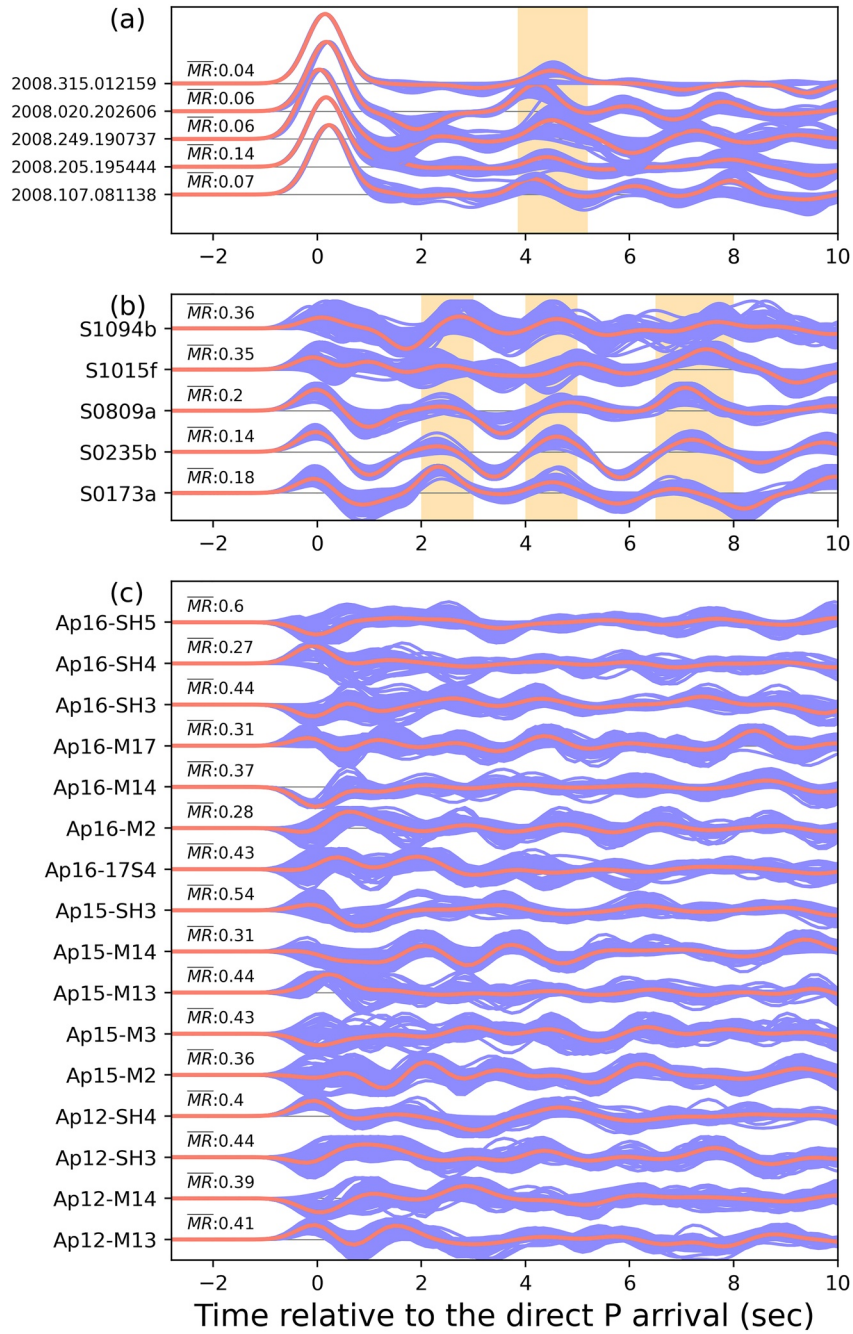

Figure 5. *P*-wave receiver functions (PRFs) of Earth (a), Mars (b), and the Moon (c). The PRFs are computed from the seismic waveforms shown in Figure 2. The *Y*-axis is shown in the same manner as Figure 2. For each event, we calculate 85 PRFs (solid purple lines) using 85 different time windows that span from 10 s before to 15–100 s after the direct *P* wave. The solid pink line represents the average stacked PRF of each event. For Earth (panel a), we highlight the possible crustal converted phase with an orange-shaded box, and for Mars (panel b), we indicate the three converted phases detected in previous studies (Durán et al., 2022; Knapmeyer-Endrun et al., 2021; Lognonné et al., 2020) with three orange-shaded boxes as well. The left side of each RF displays the average misfit reduction ($\overline{MR}$) of the 85 PRFs between the predicted and real radial components.

On Earth, we calculate the average MR of stacked PRFs from all seismic stations in each planetary field analog, as listed in Table 1. The Earth's PRFs have average MRs ranging from ∼0.1 to 0.24. Specifically, the lowest average MR (∼0.1) is found in the Grenville Province (GP), with the anorthosite massifs located in the Cana-

dian shield, which has a simple crustal structure and few scatterers. In contrast, volcanic areas tend to have larger average MRs (>0.15) due to the complex crustal structure and many scatterers. The highest average MR (0.24) is observed in the Andes Mountains of Argentina, probably due to the more complex crustal structure shaped by the subduction and compression of the eastern Pacific plate and more scatterers caused by the volcanism. In the sedimentary (Qaidam) and evaporitic (MSP) basins, the average MRs range from 0.1 to 0.15. The overall MR of Earth's PRFs is small, indicating that Earth's PRFs are reliable and that most converted waves can be recovered.

On Mars, the MRs of the PRFs are only slightly larger than those of Earth's PRFs, with an average value of approximately 0.25, suggesting that the PRFs of Mars are stable and reliable as well. The stacked PRFs of the five marsquake events show four consistent positive signals within 10 s (Figure 5b). The first signal at zero lag time represents the direct *P* wave, while the subsequent signals at approximately 2.5, 5, and 7 s may denote the converted *S* waves of the intra-crustal or crust–mantle boundaries (highlighted in orange-shaded boxes in Figure 5b). Previous studies have also detected these three converted waves using different techniques and events (Durán et al., 2022; Knapmeyer-Endrun et al., 2021; Lognonné et al., 2020).

In contrast, on the Moon, the large average MR (∼0.4) demonstrates that most of the Moon's PRFs are unreliable. The stacked PRFs between different moonquake events vary greatly (Figure 5c). There are few consistent signals for the PRFs in the same station, including the direct *P* wave. The direct *P* waves of the Moon's PRFs could be very weak in amplitude or appear positive and negative in polarity, indicating a large uncertainty even for the direct *P* wave. Additionally, Figure 5c reveals that the PRF of each moonquake event, calculated using different time windows, is generally unstable, as evident from the noticeable variations in the purple lines.

The PRF stability of the three planetary bodies differs due to their distinct crustal scattering properties, as the PRF is sensitive to the crustal structure near the station. To determine the main factor influencing the PRF stability, we compute stacked PRFs from synthetic seismograms using velocity models of the three planetary bodies (refer to Table S1 in Supporting Information S1) incorporating varying scattering media. We test two values of a, the same as in Figure 4: 1,000 m, which is less than half the seismic wavelengths of the three planetary bodies investigated in this study (Earth: 6,720 m, Mars: 3,700 m, and the Moon: 3,600 m) or equal to the wavelength of moonquakes (1,000 m) if Moon's low-velocity regolith is taken into account; 4,000 m, which is comparable to the wavelength of marsquakes or the wavelength of the moonquakes without the low-velocity regolith. Meanwhile, we assign ε of 0.05, 0.1, 0.2, and 0.25, with the 0.25 of ε corresponding to a velocity fluctuation of about ±100%. We perform experiments with different combinations of scattering parameters and obtain an average stacked PRF and 2σ uncertainty with 20 distinct media generated by random seeds (e.g., Figure S4 in Supporting Information S1). To assess the reliability and stability of the synthetic PRF, we also calculate the average MR with 2σ for the synthetic PRF. The ray parameters of the synthetic PRFs are the same as the average ray parameters of the selected earthquakes (∼0.06 s/km), marsquakes (∼0.12 s/km), and moonquakes (∼0.08 s/km). Note that the ray parameter of synthetic seismic waveforms does not affect the result because we reach a similar outcome when we use different ray parameters (e.g., Figure S5 in Supporting Information S1). In addition, we obtain a similar result from the 3D seismic wave simulation (e.g., Figure S6 in Supporting Information S1) and the teleseismic wave simulation (e.g., Figure S7 in Supporting Information S1). Considering the computational cost, we focus on the 2D case and simulate the plane wave near the receiver.

The synthetic PRFs show less influence due to the a, whereas the ε is identified as the main factor affecting PRF stability (Figure 6). As the ε increases, the stability of the stacked PRFs of the three planetary bodies degrades, and the MR of a PRF increases (Figure 7). When ε is equal to 0.2, the average MRs of synthetic PRFs for the three planetary bodies are approximately 0.2 (Earth), 0.32 (Mars), and 0.38 (the Moon). For the observed PRFs, the average MR of PRFs calculated from the eight planetary field analogs on Earth is about 0.17 (Table 1), and the average MRs below the InSight lander and the Apollo stations are ∼0.25 (Figure 5b) and ∼0.4 (Figure 5c). Therefore, we estimate that the ε value of the shallow crust of Earth and beneath the InSight lander on Mars is less than ∼0.2, but for the shallow crust beneath the Apollo stations on the Moon, it is estimated to be greater than ∼0.2 (Figure 7).

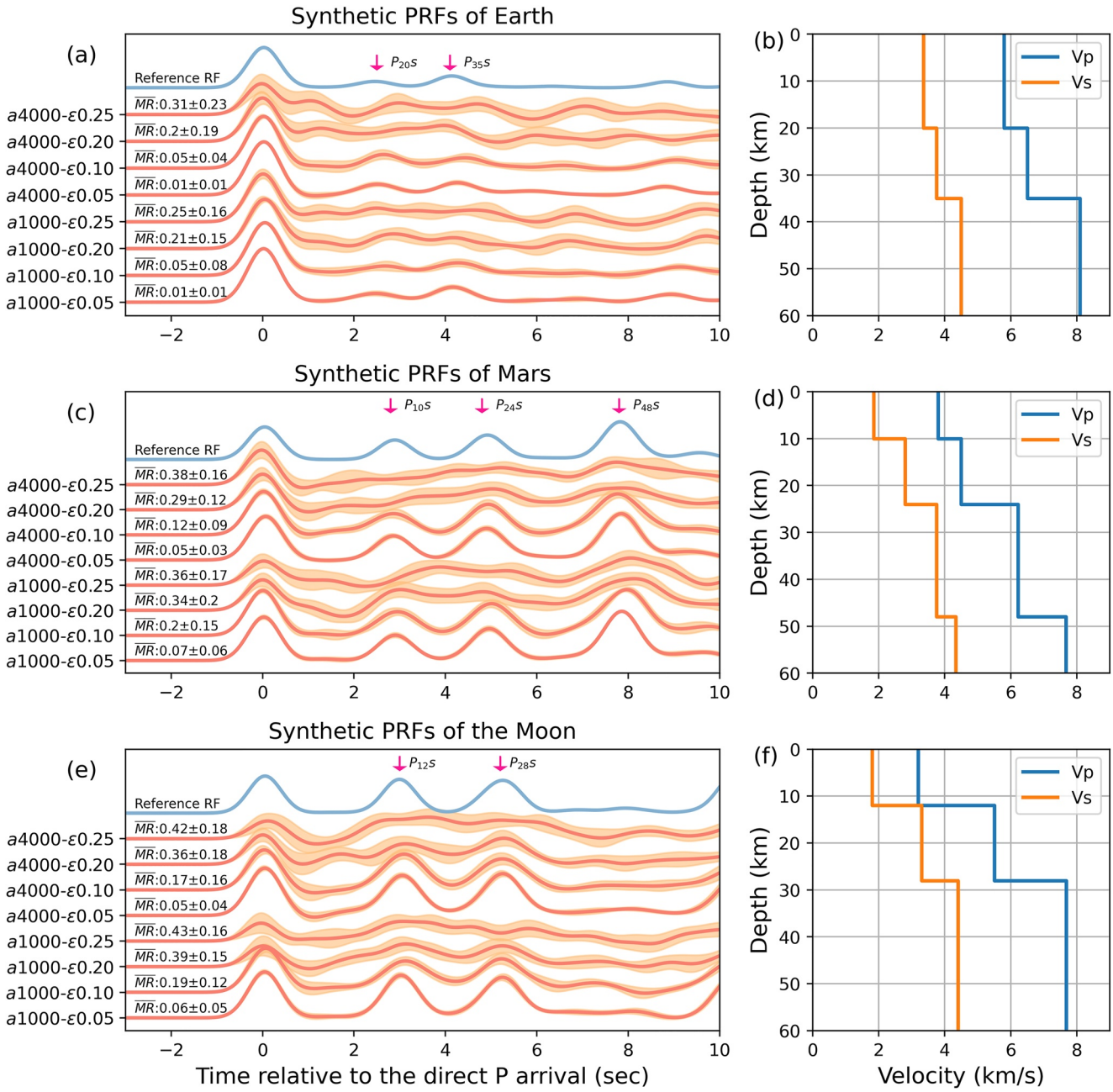

Figure 6. Synthetic stacked *P*-wave receiver functions (PRFs) and velocity models of Earth (a and b), Mars (c and d), and the Moon (e and f) with different scattering media. In the synthetic PRFs (a, c, and e), the solid orange lines and shaded areas represent the average PRFs and their associated 2σ uncertainties, respectively. The solid light blue line represents the PRF of a layered homogeneous medium for reference. The *Y*-axis labels the correlation length (a) and fractional velocity fluctuation (ε) corresponding to each PRF. On the left side, we display the average misfit reduction ($\overline{\text{MR}}$) of each PRF with its 2σ uncertainty. The pink arrows indicate the theoretically converted waves from the corresponding velocity model.

4. Discussion

Our results indicate that the seismic scattering in the shallow crust of the Moon is stronger than that of Earth and Mars. The difference in the scattering properties of the three planetary bodies mainly lies in the different fractional velocity fluctuations in their shallow crusts. For the Earth's shallow crust, the estimated fractional velocity fluctuation ($\varepsilon < \sim 0.2$) is compatible with the results of previous studies (Flatté & Wu, 1988; Fukushima, 2003; Nakata & Beroza, 2015; Wu et al., 1994), where ε values range from ~0.01 to 0.2. For the ε value of the Martian shallow crust, although not previously reported, a different method of multiscattering analysis of earthquakes, marsquakes, and moonquakes confirms

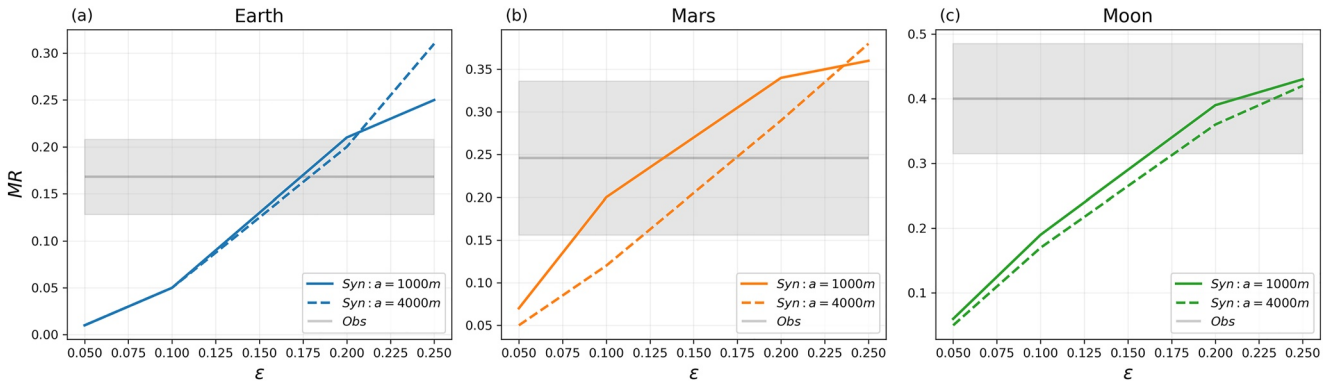

Figure 7. Variation of the misfit reduction (MR) of the P-wave receiver function of Earth (a), Mars (b), and the Moon (c) with the fractional velocity fluctuation (ε) of the scattering medium. In each panel, we plot the MR of synthetic PRFs corresponding to the correlation length (a) of 1,000 m (solid line) and 4,000 m (dashed line). We mark the average MR of observed PRFs with the solid gray line and the associated 1σ with the shaded gray area.

that the strength of the crustal seismic scattering of Mars is Earth-like (Menina et al., 2021), but is weaker than that of the Moon (Lognonné et al., 2020). This can also be verified by surface waves, which have been observed in the event waveforms of marsquakes (Charalambous et al., 2022; Kim et al., 2022; Z. Xu et al., 2023) but have never been detected in moonquakes. This is because strong scattering results in the rapid diffusion of surface-wave energy to that of scattered body waves, leading to the absence of surface waves (e.g., Onodera et al., 2022). For the Moon, previous seismic studies also prefer the large velocity fluctuation in the shallow crust. Zhang et al. (2022) constrain the maximum perturbation of the Moon to be at least 50%, within which the velocity perturbation is uniformly distributed, and the magnitude decays exponentially with depth. Blanchette-Guertin et al. (2015) set a random perturbation of an average of ±35% of the background model. Weber et al. (2015) and Onodera et al. (2021) mention that they present 25% and 28% velocity fluctuations in the regolith and 14% in the megaregolith.

Throughout the rest of this section, we delve deeper into the factors that may affect the estimation of the ε value, including the velocity model, the SNR, and the seismic anisotropy, as well as explore potential mechanisms that could account for the observed differences in fractional velocity fluctuations in the shallow crusts of Earth, Mars, and the Moon.

4.1. Influence of the Velocity Model

The simulation results reveal that the estimation of the ε value may be influenced by the velocity model. For example, when ε is 0.2, the MRs of the stacked synthetic PRFs (shown in Figure 6) are different for the velocity models of Earth (~0.2), Mars (~0.3), and the Moon (~0.4). Therefore, it is necessary to check the influence of the velocity model on the result. For the Moon, both the thickness of the low-velocity layer and the megaregolith of the lunar crust are disputed. The former can range from zero to several kilometers (Garcia et al., 2011, 2019; Onodera et al., 2021), and the latter could be more than tens of kilometers (Gillet et al., 2017; Hiesinger, 2006; Jaumann et al., 2012). Therefore, we test two additional cases for the Moon (Figure 8): case 1 features two scattering layers with a 10-km low-velocity layer (regolith) (Vp: 1 km/s; vs.: 0.5 km/s) atop a 10-km megaregolith (Figure 8b); in case 2, we set a 20-km thick megaregolith (Figure 8d). In both cases, we slightly increased the depth of the crust-mantle boundary to 35 km to prevent overlapping of the converted waves of the 20 km and the crustal-mantle discontinuities in the PRF.

For case 1, the synthetic PRFs in a layered homogeneous medium show that the crustal converted waves can be recovered (Figure S8 in Supporting Information S1), suggesting that the low-velocity layer does not act as a waveguide layer, impeding the generation of the converted waves. Subsequently, we assign the same ε value to both the regolith and the megaregolith, and compute the synthetic PRFs with various scattering media (Figure 8). The resulting synthetic PRFs of Case 1 (Figure 8a) indicate that when ε is small (<0.2), the three crustal converted waves can be extracted, but when ε reaches 0.2, the PRFs are unreliable, and the associated MR of the PRF is approximately 0.4. Similar results are observed for Case 2, where the PRF becomes unstable for values of ε greater than 0.2, and a similar MR is obtained (~0.4 when $\varepsilon = 0.2$) (Figure 8c). Therefore, the low-velocity layer and the thickness of the scattering layer of the Moon have little effect on the ε estimation of the lunar crust, and the stability of the PRF is primarily affected by the fractional velocity fluctuation of the scattering medium.

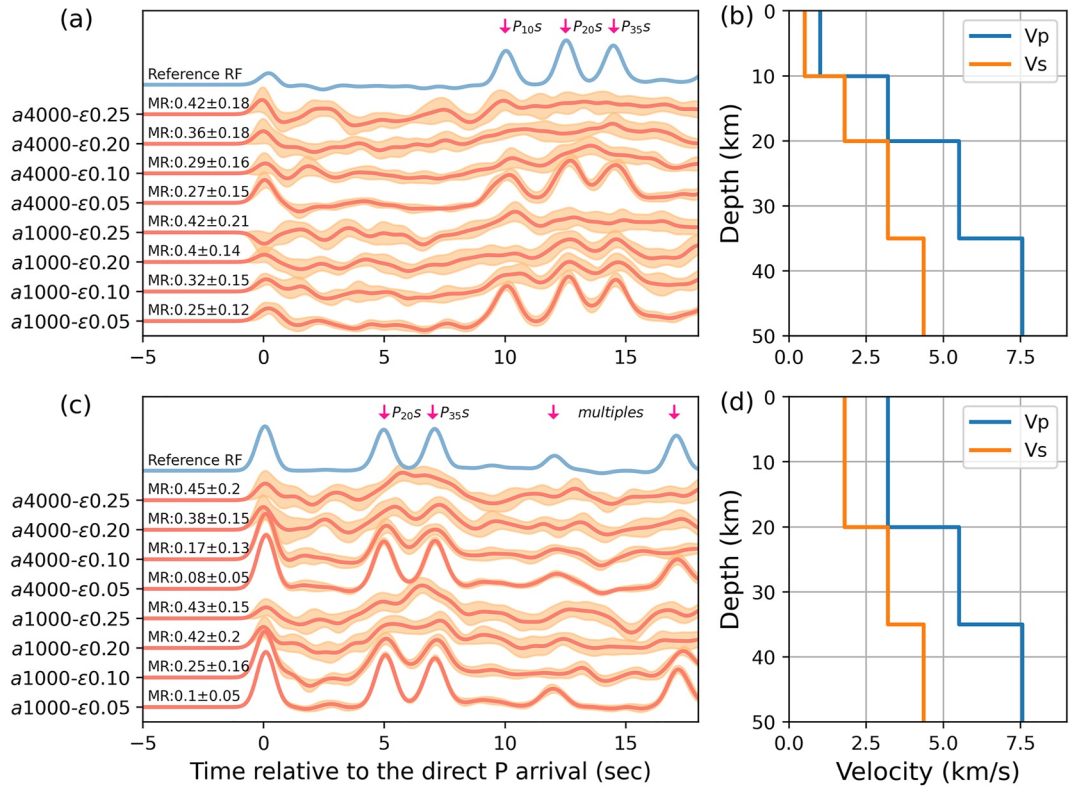

Figure 8. Synthetic stacked *P*-wave receiver functions (PRFs) for two additional crustal velocity models of the Moon with different scattering media. The figure is plotted in the same way as Figure 6. (a) Shows synthetic PRFs for a model with a 10-km low-velocity layer atop of a 10-km megaregolith (b). (c) Displays synthetic PRFs for a 20-km megaregolith model (d).

4.2. Influence of the Signal-To-Noise Ratio

The waveform quality of marsquakes and moonquakes appears to be inferior to that of earthquakes (Figure 2). To investigate whether the instabilities of PRFs observed in this study are attributable to low waveform quality, we conduct an experiment in which we generate synthetic noise based on the amplitude spectrum of the real seismic noise from the three planetary bodies. Specifically, for each planetary body, we stack the amplitude spectrum of the real seismic noise (100 s before the direct *P* wave) from all selected events to obtain the average amplitude spectrum. We then use the phase spectrum of random noise and the amplitude spectrum of the real noise to generate the synthetic noise (see Figure 9). Next, we add the synthetic noise, which has an amplitude spectrum similar to the real seismic noises of the three planetary bodies, to the synthetic seismograms. The SNR is controlled by setting the amplitude of the synthetic noise. Finally, to evaluate the quality of the PRF waveforms, we compute the correlation coefficient between the PRFs calculated from noise-containing and noise-free waveforms. We repeat this procedure 50 times for each amplitude level of noise and compute the average SNR and correlation coefficient. Figure 10 shows that the correlation coefficient between the PRFs calculated from the noise-containing and noise-free waveforms increases as the SNR increases. The PRF is reliable when the SNR of the direct *P* wave is higher than 6.0 dB because the correlation coefficient with the PRF calculated from noise-free seismograms is approximately 0.9. This result is also consistent with the outcome obtained from the addition of synthetic Gaussian noise being added.

To further rule out the possibility that real seismic noise is polarized or correlated in the three seismic components, affecting the PRF stability, we also test the influence of real seismic noise on PRF recovery. First, we cut the 100-s real seismic noise (a 100-s time window before the direct *P* wave) in the radial and vertical components for the selected seismic event waveforms (Figure S9 in Supporting Information S1); Second, we normalize the real seismic noise of each trace according to its maximum value; Third, we add the real seismic noise of Earth, Mars, and the Moon to the synthetic seismograms of the corresponding planetary body. The SNR is controlled by setting the amplitude of the seismic noise. Finally, we compute the correlation coefficient between the PRFs

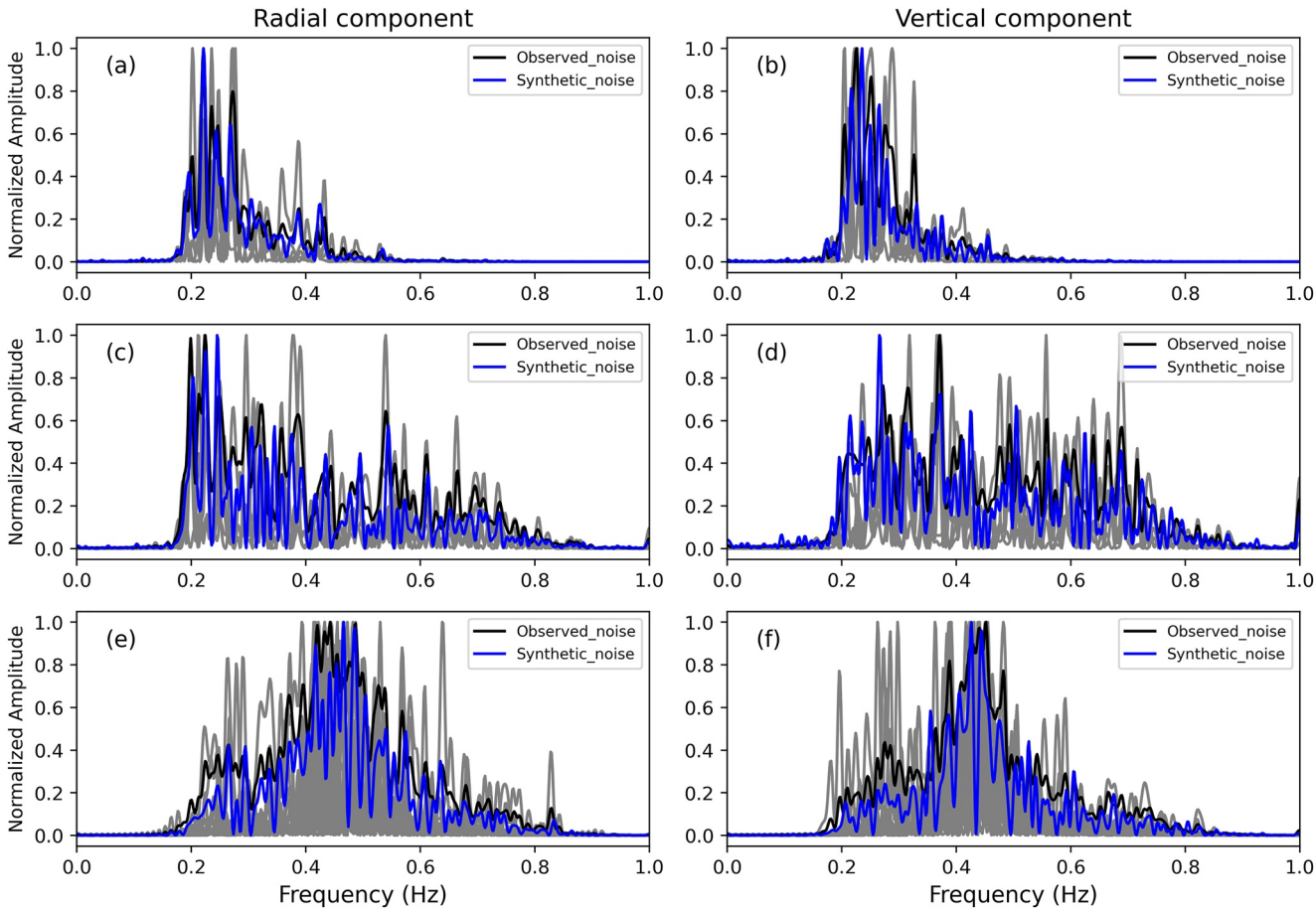

Figure 9. The normalized noise amplitude spectrum of the radial and vertical components for seismic noise which is obtained from real seismic data of Earth (a and b), Mars (c and d), and the Moon (e and f). The noise data correspond to the 100 s before the direct *P* wave for selected events shown in Figure 2. The solid gray and black lines represent the amplitude spectrum of the real seismic noise for each event and the average amplitude spectrum, respectively. The blue lines represent the amplitude spectrum of synthetic random noise.

calculated from noise-containing and noise-free waveforms. Figure S10 in Supporting Information S1 demonstrates that the average correlation coefficients are more than approximately 0.85, and the PRF is stable when the SNR reaches 6.0 dB. Therefore, we select events with the direct *P* wave SNR greater than 6.0 dB in this paper, excluding the influence of waveform quality on the PRF stability.

Another fact that supports excluding the waveform quality factor is that the Moon' PRFs are unstable and unreliable even if the SNR is very high. The PRFs calculated from marsquakes are generally stable, and the average SNR of the marsquakes used in this study is 13.75 dB, as shown in Figures 2c and 2d. In contrast, although the SNRs in both radial and vertical components of moonquakes M13 (in Apollo 15: 25.09 and 7.85 dB), M14 (in Apollo 16: 39.31 and 18.84 dB), and SH4 (in Apollo 16: 18.64 and 14.8 dB) are already higher than 13.75 dB (as shown in Figures 2e and 2f), the PRFs calculated from these three moonquake events are unstable and exhibit dramatically different waveforms, as depicted in Figure 5c. Therefore, the instability of the lunar PRF observed in this paper cannot be attributed to the waveform quality.

4.3. Influence of Seismic Anisotropy

Seismic anisotropy can affect the PRF by causing systematic variations in the arrival time, amplitude, and polarity of the converted waves based on the back azimuth of the seismic event (Nagaya et al., 2008). Seismic anisotropy is common in the Earth's crust (e.g., Han et al., 2020), and it has been detected in the Martian crust on the InSight lander (J. Li et al., 2022) as well as weak azimuthal anisotropy in the lunar subsurface (0–1 km depth) at the Apollo 14 site (Nishitsuji et al., 2020). Thus, it is reasonable to suspect that similar PRF waveforms for selected marsquake events

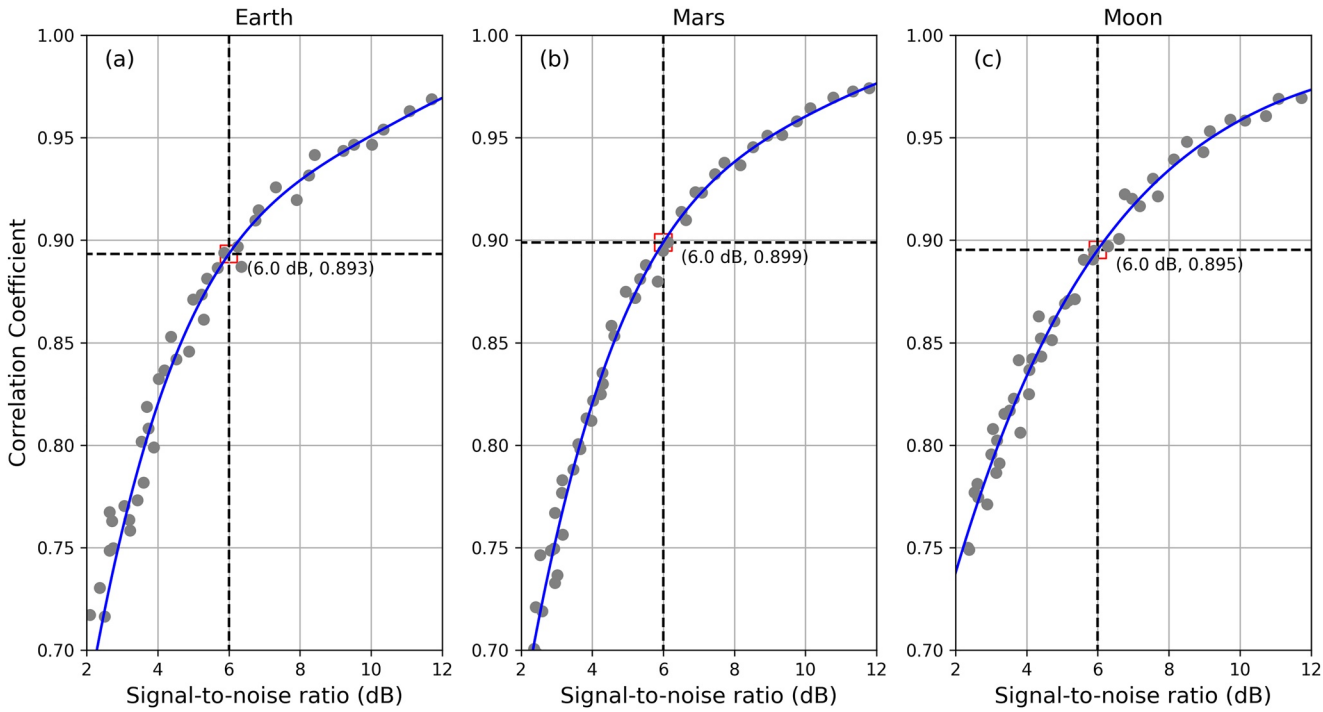

Figure 10. The correlation coefficient between *P*-wave receiver functions calculated from noise-containing and noise-free seismograms varies with the signal-to-noise ratio (SNR) of the direct *P* wave. The discrete gray point represents the average SNR and correlation coefficient of 50 simulations, and the solid blue line is the fourth-order fitting cure for these data points. The hollow red box denotes the correlation coefficient corresponding to an SNR of 6.0 dB.

are because the back azimuths of all marsquakes used in this study are concentrated within 40–90° (Figure 1b). However, seismic anisotropy cannot explain the instabilities of the PRFs of the Moon for the following three reasons: (a) the back azimuths of moonquake events M17 (~293°) and SH5 (~295°) from Apollo 16 are very close to each other, yet the PRFs calculated from the two events are unstable and dramatically different, with direct *P* waves of opposite polarity (Figure 5c); (b) seismic anisotropy may influence the amplitude of the direct *P* wave in the radial PRF without changing its polarity. However, there are direct *P* waves with negative polarity in some PRFs of the Moon; (c) it is unclear whether crustal seismic anisotropy exists beneath the Apollo stations used in this paper. Therefore, the instability of the PRFs of the Moon is independent of the seismic anisotropy.

4.4. Mechanism of the Different Fractional Velocity Fluctuations for the Three Planetary Bodies

This paper reveals different fractional velocity fluctuations of the shallow crusts of Earth, Mars, and the Moon. Here, we discuss three plausible mechanisms that may affect the fractional velocity fluctuation of the shallow crust of a planetary body: (a) the fractured crust generated by meteoritic impacts; (b) the compositional heterogeneity of the crustal rocks; (c) the water content of the crustal rocks.

Firstly, meteoritic impacts can crush the shallow crust and thus increase the fractional velocity fluctuation. Mars has approximately 385,000 impact craters ≥1 km in diameter (Lagain et al., 2021; Robbins & Hynek, 2012), and the Moon has approximately 1.3 million craters of similar size (Robbins, 2019). Although there are an order of magnitude more craters on the Moon than on Mars, the number of craters on Mars is still much greater than on Earth today (only 198 confirmed impact craters) (Kenkmann, 2021). Small fractional velocity fluctuations ($\varepsilon < 0.2$) in the shallow crusts of Earth and Mars suggest that meteoritic impacts are not the primary reason for explaining the ε discrepancy. This is reinforced by two observations: (a) The average MR beneath the AA on Earth (Table 1) is ~0.24, which is close to that beneath the InSight lander on Mars (~0.25). This indicates that the ε of the shallow crust beneath the AA on Earth is comparable to that beneath the InSight on Mars, while there are more craters near InSight than on Earth; (b) On the Moon, the average MR beneath Apollo 12 (~0.41) is slightly larger than that from Apollo 16 (~0.39) (i.e., a larger ε in Apollo 12 than in Apollo 16), while the number of craters near Apollo 12 is smaller than that near Apollo 16. These two observations suggest that ε does

not increase linearly with the number of impact craters; thus, the variation in fractional velocity fluctuation of the shallow crust of the three planetary bodies is not primarily due to the heterogeneity caused by meteoritic impacts.

Secondly, the compositional heterogeneity in the shallow crust may determine the velocity fluctuation since the velocity of different rocks may vary greatly (Christensen, 1996). Compositional heterogeneity may arise from volcanism or plate tectonics. Volcanism can introduce mantle-derived material into the crust and mix with crustal materials, leading to heterogeneous crustal composition (e.g., Liao et al., 2018). However, the effect of volcanism on the ε discrepancy of the three planetary bodies can be ruled out for two reasons: (a) Apollo 12 and 15, which are located in the mare regions once with massive volcanism, have the similar MR of PRFs (∼0.4) to Apollo 16 located in the highlands with rare volcanism (Wieczorek et al., 2006). (b) The Afro-Arabian region on Earth used in this study is a Large Igneous Province, and the InSight lander is also at volcanic area on Mars (Pan et al., 2020). However, their PRFs are stable and reliable and the estimated ε values are small ($\varepsilon < 0.2$), implying that volcanism-induced crustal composition heterogeneity is not the main factor. In addition, plate tectonics may contribute to the compositional heterogeneity of crustal rocks, which varies across different tectonic settings due to various geological processes. Rocks in stable tectonic areas (e.g., shield) are generally simple, whereas those in active tectonic areas are more heterogeneous (e.g., subduction zone and orogenic belt) (Rudnick & Gao, 2003). This is in agreement with our observation that the PRF is stable and the MR is small in the GP of the Canadian shield, whereas in the AA of the western pacific subduction zone, the PRF is less stable and the MR is slightly large (Table 1). However, plate tectonics cannot explain the unstable PRFs on the Moon, as there is no plate tectonics on the Moon (Jaumann et al., 2012). Furthermore, the crustal rock compositions of the three planetary bodies are similar in some places; for example, the GP on Earth (Petrescu et al., 2016) and the highlands on the Moon (Wieczorek et al., 2006) are both located on anorthosite massifs, and the surfaces of the AALIP on Earth, the Elysium Planitia on Mars, and the mare regions on the Moon are all covered by basalts. Therefore, heterogeneity of rock composition in the shallow crust cannot account for the small ε in the shallow crusts of Earth and Mars and the large ε in the shallow crust of the Moon.

Thirdly, the velocity fluctuation can be influenced by the water content of the crustal rocks. The seismic wave velocity is generally larger in wet porous media than in dry porous media (e.g., El Sayed et al., 2015; Ji et al., 2019). This is because the seismic wave velocity of a porous medium is determined by the equivalent density and equivalent elastic modulus of the medium (Kuster & Toksöz, 1974; Toksöz et al., 1976), which are larger for a wet porous medium than for a dry one. Meanwhile, the seismic velocity of porous media also decreases when the porous media is in a vacuum because seismic waves are mechanical waves (Shearer, 2009) that cannot propagate through a vacuum. Therefore, the seismic wave velocity of porous media in dry and vacuum environments deviates far from that of the groundmass of the rocks, resulting in large velocity fluctuations. On Earth, water in the upper continental crust exists in hydrous minerals or fluid inclusions, estimated to be approximately 0.9 wt% (Johnson, 2006). On Mars, geomorphic and geophysical evidence, such as deltas, alluvial fans, and a deep sedimentary structure, advocate that there was once abundant water (Hobiger et al., 2021; C. Li et al., 2022; Nazari-Sharabian et al., 2020). A recent simulation proposes that the present-day Martian crust may preserve 30%–99% of the initial water of Mars through crustal hydration (Scheller et al., 2021), and the water in the present-day Martian crust exists either as ice in pore spaces or as structural water in hydrous minerals (Carter et al., 2013; Nazari-Sharabian et al., 2020; Titus et al., 2003). The mass fraction of the water of the Martian crust is estimated to be ∼0.5–3.0 wt% based on the analysis of remote sensing and the Martian meteorites (Mustard, 2019). Furthermore, crustal seismic intrinsic attenuation on Mars (Lognonné et al., 2020) and the rock physical modeling (Manga & Wright, 2021) indicate that the Martian crust may contain some volatiles or water. In contrast, on the Moon, the plagioclases in the crust of the lunar highland present water contents of ∼6 ppm in sample 60015 and ∼2 ppm in sample 76535 (Hui et al., 2013). In addition, remote sensing analysis suggests a water content of 10–1,000 ppm in the lunar rocks and soils (Clark, 2009), also implying that the lunar crust is water-poor, and the lunar subsurface is in a vacuum environment (Colwell et al., 2007). As a result, the difference in scattering properties is most likely because the shallow crusts of Earth and Mars are hydrous, whereas the shallow lunar crust is anhydrous.

5. Conclusions

In this paper, we demonstrate that the PRF can be utilized to constrain the scattering properties of the shallow crust of a planetary body. The fractional velocity fluctuation of the shallow crust is the primary factor affecting

the reliability and stability of the PRF. Our investigations indicate that the fractional velocity fluctuation of the shallow crust on Earth and Mars is less than ~0.2, while that on the Moon is greater than ~0.2 due to its extremely dry shallow crust. Additionally, our research reveals that seismic phases in a highly scattering medium, such as on the Moon, can be significantly distorted and, therefore, unreliable. In such cases, seismic phase-based techniques, for example, the receiver function method, will not work. Therefore, suppressing or separating scattered waves is necessary to study interior seismic structures.

Data Availability Statement

The seismic data of earthquake events are downloaded from the Incorporated Research Institutions for Seismology (IRIS) Data Center and are available at Shi et al. (2023b). Seismic data of InSight SEIS are provided by InSight Mars SEIS Data Service., (2019). The seismic waveforms of moonquakes are referred to Nunn (1969). All seismic data and codes used in this study are archived in Shi et al. (2023b). The Mars Seismic Catalog is provided by the MQS (InSight Marsquake Service., 2022). The receiver functions are calculated by Seispy (M. Xu & He, 2023). Figures are plotted by Matplotlib (Hunter, 2007).

Acknowledgments

We thank editor Laurent Montesi and two anonymous reviewers for the constructive comments that helped to improve this paper, and we thank Son Pham for reviewing this article. This research is funded by the National Natural Science Foundation of China (Grants 42125303, 42174214) and the Fundamental Research Funds for the Central Universities (Grant 020614380122). Ling Chen is supported by the National Natural Science Foundation of China (42288201). Jing Shi is supported by the China Scholarship Council (No. 202106190130) and he thanks Dr. Cunrui Han for his helpful discussion. We acknowledge NASA, CNES, their partner agencies and institutions (UKSA, SSO, DLR, JPL, IPGP-CNRS, ETHZ, IC, MPS-MPG) and the flight operations team at JPL, SISMOC, MSDS, IRIS-DMC, and PDS for providing SEED SEIS data of marsquakes.

References

Aki, K., & Chouet, B. (1975). Origin of coda waves: Source, attenuation, and scattering effects. *Journal of Geophysical Research*, *80*(23), 3322–3342. https://doi.org/10.1029/JB080i023p03322

Banerdt, W. B., Smrekar, S. E., Banfield, D., Giardini, D., Golombek, M., Johnson, C. L., et al. (2020). Initial results from the InSight mission on Mars. *Nature Geoscience*, *13*(3), 183–189. https://doi.org/10.1038/s41561-020-0544-y

Blanchette-Guertin, J.-F., Johnson, C. L., & Lawrence, J. F. (2015). Effects of lateral variations in megaregolith thickness on predicted lunar seismic signals: Variations in megaregolith thickness. *Geophysical Research Letters*, *42*(23), 10171–10178. https://doi.org/10.1002/2015GL066151

Carter, J., Poulet, F., Bibring, J.-P., Mangold, N., & Murchie, S. (2013). Hydrous minerals on Mars as seen by the CRISM and OMEGA imaging spectrometers: Updated global view: Hydrous minerals on mars: Global view. *Journal of Geophysical Research: Planets*, *118*(4), 831–858. https://doi.org/10.1029/2012JE004145

Charalambous, C., Pike, T., Fernando, B., Stott, A., Nissen-Meyer, T., & Lognonné, P. (2022). Denoising InSight: Determination of Mars' lateral crustal variations through surface-wave identification (other). display. https://doi.org/10.5194/epsc2022-1078

Christensen, N. I. (1996). Poisson's ratio and crustal seismology. *Journal of Geophysical Research*, *101*(B2), 3139–3156. https://doi.org/10.1029/95JB03446

Clark, R. N. (2009). Detection of adsorbed water and hydroxyl on the Moon. *Science*, *326*(5952), 562–564. https://doi.org/10.1126/science.1178105

Colwell, J. E., Batiste, S., Horányi, M., Robertson, S., & Sture, S. (2007). Lunar surface: Dust dynamics and regolith mechanics. *Reviews of Geophysics*, *45*(2), RG2006. https://doi.org/10.1029/2005RG000184

Durán, C., Khan, A., Ceylan, S., Zenhäusern, G., Stähler, S., Clinton, J. F., & Giardini, D. (2022). Seismology on Mars: An analysis of direct, reflected, and converted seismic body waves with implications for interior structure. *Physics of the Earth and Planetary Interiors*, *325*, 106851. https://doi.org/10.1016/j.pepi.2022.106851

El Sayed, N. A., Abuseda, H., & Kassab, M. A. (2015). Acoustic wave velocity behavior for some Jurassic carbonate samples, north Sinai, Egypt. *Journal of African Earth Sciences*, *111*, 14–25. https://doi.org/10.1016/j.jafrearsci.2015.07.016

Flatté, S. M., & Wu, R.-S. (1988). Small-scale structure in the lithosphere and asthenosphere deduced from arrival time and amplitude fluctuations at NORSAR. *Journal of Geophysical Research*, *93*(B6), 6601. https://doi.org/10.1029/JB093iB06p06601

Fukushima, Y. (2003). Laboratory study on scattering characteristics of shear waves in rock samples. *Bulletin of the Seismological Society of America*, *93*(1), 253–263. https://doi.org/10.1785/0120020074

Garcia, R. F., Gagnepain-Beyneix, J., Chevrot, S., & Lognonné, P. (2011). Very preliminary reference Moon model. *Physics of the Earth and Planetary Interiors*, *188*(1–2), 96–113. https://doi.org/10.1016/j.pepi.2011.06.015

Garcia, R. F., Khan, A., Drilleau, M., Margerin, L., Kawamura, T., Sun, D., et al. (2019). Lunar seismology: An update on interior structure models. *Space Science Reviews*, *215*(8), 50. https://doi.org/10.1007/s11214-019-0613-y

Gillet, K., Margerin, L., Calvet, M., & Monnereau, M. (2017). Scattering attenuation profile of the Moon: Implications for shallow moonquakes and the structure of the megaregolith. *Physics of the Earth and Planetary Interiors*, *262*, 28–40. https://doi.org/10.1016/j.pepi.2016.11.001

Golombek, M., Grott, M., Kargl, G., Andrade, J., Marshall, J., Warner, N., et al. (2018). Geology and physical properties investigations by the InSight lander. *Space Science Reviews*, *214*(5), 84. https://doi.org/10.1007/s11214-018-0512-7

Han, C., Xu, M., Huang, Z., Wang, L., Xu, M., Mi, N., et al. (2020). Layered crustal anisotropy and deformation in the SE Tibetan plateau revealed by Markov-Chain-Monte-Carlo inversion of receiver functions. *Physics of the Earth and Planetary Interiors*, *306*, 106522. https://doi.org/10.1016/j.pepi.2020.106522

Hiesinger, H. (2006). New views of lunar geoscience: An introduction and overview. *Reviews in Mineralogy and Geochemistry*, *60*(1), 1–81. https://doi.org/10.2138/rmg.2006.60.1

Hobiger, M., Hallo, M., Schmelzbach, C., Stähler, S. C., Fäh, D., Giardini, D., et al. (2021). The shallow structure of Mars at the InSight landing site from inversion of ambient vibrations. *Nature Communications*, *12*(1), 6756. https://doi.org/10.1038/s41467-021-26957-7

Hui, H., Peslier, A. H., Zhang, Y., & Neal, C. R. (2013). Water in lunar anorthosites and evidence for a wet early Moon. *Nature Geoscience*, *6*(3), 177–180. https://doi.org/10.1038/ngeo1735

Hunter, J. D. (2007). Matplotlib: A 2D graphics environment. *Computing in Science & Engineering*, *9*(3), 90–95. https://doi.org/10.1109/MCSE.2007.55

InSight Marsquake Service. (2022). *Mars seismic catalogue, InSight mission; V12 2022-10-01. Bristol: ETHZ, IPGP, JPL, ICL, ISAE-Supaero*. MPS, University. https://doi.org/10.12686/a18

InSight Mars SEIS Data Service. (2019). Seis raw data, insight mission. *IPGP, JPL, CNES, ETHZ, ICL, MPS, ISAE-Supaero, LPG, MFSC*. https://doi.org/10.18715/SEIS.INSIGHT.XB_2016

Jarosch, H. S. (1977). The use of surface reflections in lunar seismograms. *Bulletin of the Seismological Society of America*, *67*(6), 1647–1659. https://doi.org/10.1785/BSSA0670061647

Jaumann, R., Hiesinger, H., Anand, M., Crawford, I. A., Wagner, R., Sohl, F., et al. (2012). Geology, geochemistry, and geophysics of the Moon: Status of current understanding. *Planetary and Space Science*, *74*(1), 15–41. https://doi.org/10.1016/j.pss.2012.08.019

Ji, S., Wang, Q., & Li, L. (2019). Seismic velocities, Poisson's ratios and potential auxetic behavior of volcanic rocks. *Tectonophysics*, *766*, 270–282. https://doi.org/10.1016/j.tecto.2019.06.013

Johnson, E. A. (2006). Water in nominally anhydrous crustal minerals: Speciation, concentration, and geologic significance. *Reviews in Mineralogy and Geochemistry*, *62*(1), 38–154. https://doi.org/10.2138/rmg.2006.62.6

Jolliff, B. L., Wieczorek, M. A., Shearer, C. K., & Neal, C. R. (2006). New views of the Moon. *Reviews in Mineralogy and Geochemistry*, *60*(1). https://doi.org/10.2138/rmg.2006.60.0

Kenkmann, T., & Artemieva, N. (2021). The terrestrial impact crater record: A statistical analysis of morphologies, structures, ages, lithologies, and more. *Meteoritics & Planetary Sciences*, *56*(5), 1024–1070. https://doi.org/10.1111/maps.13657

Kennett, B. L. N. (1991). IASPEI 1991 seismological tables. *Terra Nova*, *3*(2), 122. https://doi.org/10.1111/j.1365-3121.1991.tb00863.x

Khan, A., Ceylan, S., van Driel, M., Giardini, D., Lognonné, P., Samuel, H., et al. (2021). Upper mantle structure of Mars from InSight seismic data. *Science*, *373*(6553), 434–438. https://doi.org/10.1126/science.abf2966

Kim, D., Banerdt, W. B., Ceylan, S., Giardini, D., Lekić, V., Lognonné, P., et al. (2022). Surface waves and crustal structure on Mars. *Science*, *378*(6618), 417–421. https://doi.org/10.1126/science.abq7157

Knapmeyer-Endrun, B., Panning, M. P., Bissig, F., Joshi, R., Khan, A., Kim, D., et al. (2021). Thickness and structure of the Martian crust from InSight seismic data. *Science*, *373*(6553), 438–443. https://doi.org/10.1126/science.abf8966

Kumagai, H., Londoño, J. M., Maeda, Y., López Velez, C. M., & Lacson, R. (2018). Envelope widths of volcano-seismic events and seismic scattering characteristics beneath volcanoes. *Journal of Geophysical Research: Solid Earth*, *123*(11), 9764–9777. https://doi.org/10.1029/2018JB015557

Kuster, G. T., & Toksöz, M. N. (1974). Velocity and attenuation of seismic waves in two-phase media: Part I. Theoretical formulations. *Geophysics*, *39*(5), 587–606. https://doi.org/10.1190/1.1440450

Lagain, A., Bouley, S., Baratoux, D., Marmo, C., Costard, F., Delaa, O., et al. (2021). Mars Crater database: A participative project for the classification of the morphological characteristics of large Martian craters. In W. U. Reimold, & C. Koeberl (Eds.), *Large meteorite impacts and planetary evolution VI* (pp. 629–644). Geological Society of America. https://doi.org/10.1130/2021.2550(29)

Langston, C. A. (1979). Structure under Mount Rainier, Washington, inferred from teleseismic body waves. *Journal of Geophysical Research*, *84*(B9), 4749. https://doi.org/10.1029/JB084iB09p04749

Latham, G. V., Ewing, M., Press, F., Sutton, G., Dorman, J., Nakamura, Y., et al. (1970). Passive seismic experiment. *Science*, *167*(3918), 455–457. https://doi.org/10.1126/science.167.3918.455

Li, C., Zheng, Y., Wang, X., Zhang, J., Wang, Y., Chen, L., et al. (2022). Layered subsurface in Utopia Basin of Mars revealed by Zhurong rover radar. *Nature*, *610*(7931), 308–312. https://doi.org/10.1038/s41586-022-05147-5

Li, J., Beghein, C., Wookey, J., Davis, P., Lognonné, P., Schimmel, M., et al. (2022). Evidence for crustal seismic anisotropy at the InSight lander site. *Earth and Planetary Science Letters*, *593*, 117654. https://doi.org/10.1016/j.epsl.2022.117654

Liao, J.-P., Jahn, B.-M., Alexandrov, I., Chung, S.-L., Zhao, P., Ivin, V., & Usuki, T. (2018). Petrogenesis of Mid-Eocene granites in South Sakhalin, Russian Far East: Juvenile crustal growth and comparison with granitic magmatism in Hokkaido and Sikhote-Alin. *Journal of Asian Earth Sciences*, *167*, 103–129. https://doi.org/10.1016/j.jseaes.2018.05.020

Ligorria, J. P., & Ammon, C. J. (1999). Iterative deconvolution and receiver-function estimation. *Iterative Deconvolution and Receiver-Function Estimation*, *89*(5), 1395–1400. https://doi.org/10.1785/BSSA0890051395

Lognonné, P., Banerdt, W. B., Giardini, D., Pike, W. T., Christensen, U., Laudet, P., et al. (2019). SEIS: Insight's seismic experiment for internal structure of Mars. *Space Science Reviews*, *215*(1), 12. https://doi.org/10.1007/s11214-018-0574-6

Lognonné, P., Banerdt, W. B., Pike, W. T., Giardini, D., Christensen, U., Garcia, R. F., et al. (2020). Constraints on the shallow elastic and anelastic structure of Mars from InSight seismic data. *Nature Geoscience*, *13*(3), 213–220. https://doi.org/10.1038/s41561-020-0536-y

Lognonné, P., Gagnepain-Beyneix, J., & Chenet, H. (2003). A new seismic model of the Moon: Implications for structure, thermal evolution and formation of the Moon. *Earth and Planetary Science Letters*, *211*(1–2), 27–44. https://doi.org/10.1016/S0012-821X(03)00172-9

Maeda, T., Takemura, S., & Furumura, T. (2017). OpenSWPC: An open-source integrated parallel simulation code for modeling seismic wave propagation in 3D heterogeneous viscoelastic media. *Earth Planets and Space*, *69*(1), 102. https://doi.org/10.1186/s40623-017-0687-2

Manga, M., & Wright, V. (2021). No cryosphere-confined aquifer below InSight on Mars. *Geophysical Research Letters*, *48*(8), e2021GL093127. https://doi.org/10.1029/2021GL093127

Margerin, L. (2011). Seismic waves, scattering. *Encyclopedia of Earth Sciences Series*, 1210–1223. https://doi.org/10.1007/978-90-481-8702-7_54

Menina, S., Margerin, L., Kawamura, T., Lognonné, P., Marti, J., Drilleau, M., et al. (2021). Energy envelope and attenuation characteristics of high-frequency (HF) and very-high-frequency (VF) Martian events. *Bulletin of the Seismological Society of America*, *111*(6), 3016–3034. https://doi.org/10.1785/0120210127

Mustard, J. F. (2019). Sequestration of volatiles in the Martian crust through hydrated minerals. In *Volatiles in the Martian crust* (pp. 247–263). Elsevier. https://doi.org/10.1016/B978-0-12-804191-8.00008-8

Nagaya, M., Oda, H., Akazawa, H., & Ishise, M. (2008). Receiver functions of seismic waves in layered anisotropic media: Application to the estimate of seismic anisotropy. *Bulletin of the Seismological Society of America*, *98*(6), 2990–3006. https://doi.org/10.1785/0120080130

Nakamura, Y. (2005). Farside deep moonquakes and deep interior of the Moon. *Journal of Geophysical Research*, *110*(E1), E01001. https://doi.org/10.1029/2004JE002332

Nakata, N., & Beroza, G. C. (2015). Stochastic characterization of mesoscale seismic velocity heterogeneity in Long Beach, California. *Geophysical Journal International*, *203*(3), 2049–2054. https://doi.org/10.1093/gji/ggv421

National Geophysical Data Center. (1993). *5-minute gridded global relief data (ETOPO5)*. National Geophysical Data Center, NOAA. https://doi.org/10.7289/V5D798BF

Nazari-Sharabian, M., Aghababaei, M., Karakouzian, M., & Karami, M. (2020). Water on Mars—A literature review. *Galaxies*, *8*(2), 40. https://doi.org/10.3390/galaxies8020040

Nishitsuji, Y., Ruigrok, E., & Draganov, D. (2020). Azimuthal anisotropy of the megaregolith at the Apollo 14 landing site. *Journal of Geophysical Research: Planets*, *125*(5), e2019JE006126. https://doi.org/10.1029/2019JE006126

Nunn, C. (1969). Apollo passive seismic experiments [Dataset]. International Federation of Digital Seismograph Networks. https://doi.org/10.7914/SN/XA_1969

Nunn, C., Garcia, R. F., Nakamura, Y., Marusiak, A. G., Kawamura, T., Sun, D., et al. (2020). Lunar seismology: A data and instrumentation review. *Space Science Reviews*, *216*(5), 89. https://doi.org/10.1007/s11214-020-00709-3

Onodera, K., Kawamura, T., Tanaka, S., Ishihara, Y., & Maeda, T. (2021). Numerical simulation of lunar seismic wave propagation: Investigation of subsurface scattering properties near Apollo 12 landing site. *Journal of Geophysical Research: Planets*, *126*(3), e2020JE006406. https://doi.org/10.1029/2020JE006406

Onodera, K., Kawamura, T., Tanaka, S., Ishihara, Y., & Maeda, T. (2022). Quantitative evaluation of the lunar seismic scattering and comparison between the Earth, Mars, and the Moon. *Journal of Geophysical Research: Planets*, *127*(12), e2022JE007558. https://doi.org/10.1029/2022JE007558

Pan, L., Quantin-Nataf, C., Tauzin, B., Michaut, C., Golombek, M., Lognonné, P., et al. (2020). Crust stratigraphy and heterogeneities of the first kilometers at the dichotomy boundary in western Elysium Planitia and implications for InSight lander. *Icarus*, *338*, 113511. https://doi.org/10.1016/j.icarus.2019.113511

Petrescu, L., Bastow, I. D., Darbyshire, F. A., Gilligan, A., Bodin, T., Menke, W., & Levin, V. (2016). Three billion years of crustal evolution in eastern Canada: Constraints from receiver functions. *Journal of Geophysical Research: Solid Earth*, *121*(2), 788–811. https://doi.org/10.1002/2015JB012348

Robbins, S. J. (2019). A new global database of lunar impact craters >1–2 km: 1. Crater locations and sizes, comparisons with published databases, and global analysis. *Journal of Geophysical Research: Planets*, *124*(4), 871–892. https://doi.org/10.1029/2018JE005592

Robbins, S. J., & Hynek, B. M. (2012). A new global database of Mars impact craters ≥1 km: 1. Database creation, properties, and parameters: Mars crater database-construction. *Journal of Geophysical Research*, *117*(E5), E05004. https://doi.org/10.1029/2011JE003966

Rudnick, R. L., & Gao, S. (2003). Composition of the continental crust. *Treatise on Geochemistry*, *3*, 1–64. https://doi.org/10.1016/b0-08-043751-6/03016-4

Sato, H. (2019). Power spectra of random heterogeneities in the solid Earth. *Solid Earth*, *10*(1), 275–292. https://doi.org/10.5194/se-10-275-2019

Sato, H., Fehler, M. C., & Maeda, T. (2012). *Seismic wave propagation and scattering in the heterogeneous Earth* (2nd ed.). Springer Berlin Heidelberg. https://doi.org/10.1007/978-3-642-23029-5

Scheller, E. L., Ehlmann, B. L., Hu, R., Adams, D. J., & Yung, Y. L. (2021). Long-term drying of Mars by sequestration of ocean-scale volumes of water in the crust. *Science*, *372*(6537), 56–62. https://doi.org/10.1126/science.abc7717

Shearer, P. M. (2009). *Introduction to seismology* (2nd ed., pp. 39–64). Cambridge University Press. Chapter 3. https://doi.org/10.1017/CBO9780511841552.005

Shi, J., Plasman, M., Knapmeyer-Endrun, B., Xu, Z., Kawamura, T., Lognonné, P., et al. (2023a). High-frequency receiver functions with event S1222a reveal a discontinuity in the Martian shallow crust. *Geophysical Research Letters*, *50*(5), e2022GL101627. https://doi.org/10.1029/2022GL101627

Shi, J., Wang, T., Chen, H., Yang, M., Chen, L., Hui, H., et al. (2023b). Differences in scattering properties of the shallow crusts of Earth, Mars, and the Moon revealed by P-wave receiver functions [Dataset]. Zenodo. https://doi.org/10.5281/zenodo.7939796

Sivaji, C., Nishizawa, O., Kitagawa, G., & Fukushima, Y. (2002). A physical-model study of the statistics of seismic waveform fluctuations in random heterogeneous media: Seismic waves in random heterogeneous media. *Geophysical Journal International*, *148*(3), 575–595. https://doi.org/10.1046/j.1365-246x.2002.01606.x

Smith, D. E., Zuber, M. T., Frey, H. V., Garvin, J. B., Head, J. W., Muhleman, D. O., et al. (2001). Mars Orbiter Laser Altimeter: Experiment summary after the first year of global mapping of Mars. *Journal of Geophysical Research*, *106*(E10), 23689–23722. https://doi.org/10.1029/2000je001364

Smith, D. E., Zuber, M. T., Neumann, G. A., & Lemoine, F. G. (1997). Topography of the Moon from the clementine lidar. *Journal of Geophysical Research*, *102*(E1), 1591–1611. https://doi.org/10.1029/96JE02940

Stähler, S. C., Khan, A., Banerdt, W. B., Lognonné, P., Giardini, D., Ceylan, S., et al. (2021). Seismic detection of the Martian core. *Science*, *373*(6553), 443–448. https://doi.org/10.1126/science.abi7730

Thompson, T., & Cane, R. (2022). Educational resources for EPN24 planetary field analogue sites (other). *Oral*. https://doi.org/10.5194/epsc2022-612

Titus, T. N., Kieffer, H. H., & Christensen, P. R. (2003). Exposed water ice discovered near the South Pole of Mars. *Science*, *299*(5609), 1048–1051. https://doi.org/10.1126/science.1080497

Toksöz, M. N., Cheng, C. H., & Timur, A. (1976). Velocities of seismic waves in porous rocks. *Geophysics*, *41*(4), 621–645. https://doi.org/10.1190/1.1440639

Victor, T., Julià, J., White, N. J., & Rodríguez-Tribaldos, V. (2020). Joint inversion of high-frequency receiver functions and surface-wave dispersion: Case study in the Parnaíba Basin of northeast Brazil. *Bulletin of the Seismological Society of America*, *110*(3), 1372–1386. https://doi.org/10.1785/0120190203

Vinnik, L., Chenet, H., Gagnepain-Beyneix, J., & Lognonné, P. (2001). First seismic receiver functions on the Moon. *Geophysical Research Letters*, *28*(15), 3031–3034. https://doi.org/10.1029/2001GL012859

Weber, R. C., Knapmeyer, M., Panning, M., & Schmerr, N. (2015). Modeling approaches in planetary seismology. In V. C. H. Tong, & R. A. García (Eds.), *Extraterrestrial seismology* (1st ed., pp. 140–156). Cambridge University Press. https://doi.org/10.1017/CBO9781107300668.013

Wieczorek, M. A., Jolliff, B. L., Khan, A., Pritchard, M. E., Weiss, B. P., Williams, J. G., et al. (2006). The constitution and structure of the lunar interior. *Reviews in Mineralogy and Geochemistry*, *60*(1), 221–364. https://doi.org/10.2138/rmg.2006.60.3

Wu, R.-S., Xu, Z., & Li, X.-P. (1994). Heterogeneity spectrum and scale-anisotropy in the upper crust revealed by the German Continental Deep-Drilling (KTB) Holes. *Geophysical Research Letters*, *21*(10), 911–914. https://doi.org/10.1029/94GL00772

Xu, M., & He, J. (2023). Seispy: Python module for batch calculation and postprocessing of receiver functions. *Seismological Research Letters*, *94*(2A), 935–943. https://doi.org/10.1785/0220220288

Xu, M., Huang, H., Huang, Z., Wang, P., Wang, L., Xu, M., et al. (2018). Insight into the subducted Indian slab and origin of the Tengchong volcano in SE Tibet from receiver function analysis. *Earth and Planetary Science Letters*, *482*, 567–579. https://doi.org/10.1016/j.epsl.2017.11.048

Xu, Z., Broquet, A., Fuji, N., Kawamura, T., Lognonné, P., Montagner, J., et al. (2023). Investigation of Martian regional crustal structure near the dichotomy using S1222a surface-wave group velocities. *Geophysical Research Letters*, *50*(8), e2023GL103136. https://doi.org/10.1029/2023GL103136

Zhang, X., Zhang, L., Zhang, J., & Mitchell, R. N. (2022). Strong heterogeneity in shallow lunar subsurface detected by Apollo seismic data. *Journal of Geophysical Research: Planets*, *127*(11), e2022JE007222. https://doi.org/10.1029/2022JE007222

Zhu, L. P., & Kanamori, H. (2000). Moho depth variation in southern California from teleseismic receiver functions. *Journal of Geophysical Research*, *105*(B2), 2969–2980. https://doi.org/10.1029/1999JB900322